Unraveling electron liberation from Bi^{2+} for designing Bi^{3+}-based afterglow phosphor for anti-counterfeiting and flexible X-ray imaging

Lyu, Tianshuai; Dorenbos, Pieter; Li, Canhua; Li, Silei; Xu, Jian; Wei, Zhanhua

DOI
10.1016/j.cej.2022.135038

Publication date
2022

Document Version
Final published version

Published in
Chemical Engineering Journal

Chemical Engineering Journal 435 (2022) 135038

Contents lists available at ScienceDirect

Chemical Engineering Journal

journal homepage: www.elsevier.com/locate/cej

Unraveling electron liberation from Bi^{2+} for designing Bi^{3+}-based afterglow phosphor for anti-counterfeiting and flexible X-ray imaging

Tianshuai Lyu [a,*], Pieter Dorenbos [b], Canhua Li [a], Silei Li [a], Jian Xu [c], Zhanhua Wei [a,*]

[a] Xiamen Key Laboratory of Optoelectronic Materials and Advanced Manufacturing, Institute of Luminescent Materials and Information Displays, College of Materials Science and Engineering, Huaqiao University, Xiamen 361021, PR China

[b] Delft University of Technology, Faculty of Applied Sciences, Department of Radiation Science and Technology, section Luminescence Materials, Mekelweg 15, 2629JB Delft, the Netherlands

[c] International Center for Young Scientists (ICYS), National Institute for Materials Science (NIMS), Tsukuba 305-0044, Japan

ARTICLE INFO

Keywords:
Bi^{2+} VRBE
Bismuth
Electron liberation from Bi^{2+}
Electron trap depth engineering
X-ray imaging

ABSTRACT

It is challenging to rational design persistent luminescence and storage phosphors with high storage capacity of electrons and holes after X-ray charging. Such phosphors have potential applications in anti-counterfeiting and X-ray imaging. Here we have combined vacuum referred binding energy diagram (VRBE) construction, photoluminescence spectroscopy, and thermoluminescence to study the trapping processes of charge carriers in $NaYGeO_4$. In $NaYGeO_4$:0.004Bi^{3+} and $NaYGeO_4$:0.004Bi^{3+},0.005Ln^{3+} (Ln = Tb or Pr), Bi^{3+} appears to act as a shallow electron trap, while Bi^{3+} and Ln^{3+} act as deep hole trapping and recombination centres. We will show how to experimentally determine the VRBE in the Bi^{2+} $^2P_{1/2}$ ground state in $NaYGeO_4$ and $NaLuGeO_4$ by thermoluminescence study. The electron trap depth produced by Bi^{3+} codopant in $NaLu_{1-x}Y_xGeO_4$:0.003Bi^{3+},0.008 Tb^{3+} can be adjusted, by increasing x, resulting in conduction band engineering. By combining Bi^{3+} as an electron trap and Bi^{3+} and Tb^{3+} as the hole traps, excellent X-ray charged afterglow phosphors were developed. The integrated TL intensity of the optimized $NaYGeO_4$:0.004Bi^{3+} and $NaYGeO_4$:0.003Bi^{3+},0.008Tb^{3+} after exposure to X-rays is about 4.5 and 1.1 times higher than that of the state-of-the-art BaFBr(I):Eu^{2+} storage phosphor. Intense initial Tb^{3+} 4f → 4f afterglow appears in $NaYGeO_4$:0.003Bi^{3+},0.008Tb^{3+} and more than 40 h afterglow is measurable in $NaYGeO_4$:0.004Bi^{3+} and $NaYGeO_4$:0.003Bi^{3+}, 0.008 Tb^{3+} after X-ray charging. We will show proof-of-concept anti-counterfeiting and X-ray imaging applications by using the developed afterglow phosphors and $CsPbI_3$ quantum dots. This work not only provides experimental evidence on the VRBE in the Bi^{2+} $^2P_{1/2}$ ground state in $NaYGeO_4$, but also shows how to design and develop good afterglow phosphors for anti-counterfeiting and X-ray imaging by deeply studying and controlling the trapping processes of charge carriers in bismuth and/or lanthanides doped inorganic compounds.

1. Introduction

Persistent luminescence, also called afterglow, is known as a self-sustained photon emission phenomenon where upon excitation source stimulation like X-rays, UV-light, or β irradiation, free electrons and holes are generated and stored in compounds. Stored charge carriers can be released at room temperature (RT) to continuously produce light emission from seconds to few days after stopping the excitation source [1–4]. Because of this unique feature, afterglow phosphors have many applications like in anti-counterfeiting[5], optical information storage [6], bacteria sterilization[7], 3D X-ray imaging[8], photocatalytic reaction[2], AC-LED[9], and mechanoluminescence material exploration[10–14]. Although many inorganic compounds have been studied, $SrAl_2O_4$:Eu^{2+},Dy^{3+} developed in 1993 is still the state-of-art afterglow phosphor due to its good afterglow intensity and duration time[15,16]. One reason for the slow development of afterglow phosphors is that many compounds were studied in a trial-and-error method and the charge carrier trapping processes are often not clear.

The charge carrier trapping and de-trapping processes are of interest in order to better unravel the afterglow mechanism and to explore and develop excellent afterglow phosphors. Generally, a persistent luminescence compound contains the compound lattice, the recombination

* Corresponding authors.
E-mail addresses: lv_tianshuai@126.com (T. Lyu), weizhanhua@hqu.edu.cn (Z. Wei).

https://doi.org/10.1016/j.cej.2022.135038
Received 27 December 2021; Received in revised form 27 January 2022; Accepted 31 January 2022
Available online 4 February 2022

centre, the electron and hole capturing centres that could be compound intrinsic defect(s) or deliberately induced dopants like Cr^{3+} or lanthanides [17,18]. Relatively shallow traps (<~0.65 eV) are needed to produce room temperature persistent luminescence. One expects that a persistent luminescence phosphor could be rationally explored and designed if the trap depths of electron and hole capturing centres can be controlled or engineered[19–21]. A good afterglow phosphor then may appear by further optimizing the compound synthesis processes.

The charge carrier trapping centres and depths can be designed by analyzing the locations of $4f^n$ ground states levels of lanthanides relative to compound bands[22,23]. A trivalent lanthanide can act as an electron capturing centre if the $4f^n$ ground state level of the corresponding divalent lanthanide is below the conduction band (CB) of the compound [15,24]. Here, the electron trapping depth is defined as the distance from the conduction band bottom to the ground state $4f^n$ level of divalent lanthanide. When the $4f^n$ ground state level locations of trivalent lanthanides are close above the valence band (VB) top, they can act as hole capturing centres[17,18,25]. The hole trapping depth can be estimated by the distance between the ground state $4f^n$ level and the top of the valence band. Apparently, the energy level locations of electron and hole capturing centres, the conduction band bottom, and the valence band top in compounds are crucial to the rational design of the electron and hole trap depths. In 2012, the so-called chemical shift model was established to construct a vacuum referred binding energy (VRBE) scheme by combining limited experimental spectroscopy data[22,26]. The VRBE scheme enables to compare the electron binding energy at the lanthanide $4f^n$ ground states levels, the conduction band bottom, and the valence band maximum in various inorganic compounds with respect to an identical reference energy[27].

Like lanthanides, bismuth can act as a charge carrier trapping centre in a compound[28]. The electronic configuration of the bismuth atom is $[Xe]4f^{14}5d^{10}6s^26p^3$. Various bismuth valence states can be formed when different outermost electrons of bismuth element are lost, such as Bi^+ (the outermost electrons are $6p^2$), Bi^{2+} ($6p^1$), Bi^{3+} ($6\ s^2$), and Bi^{4+} ($6\ s^1$) [29]. In compounds trivalent bismuth can act both as an electron capturing centre and a hole trapping centre. In ref.[30], the dual role of Bi^{3+} as electron and hole traps was first tested in La-, Y-, and $LuPO_4$ compounds. However, there is no direct evidence on the VRBE in the Bi^{2+} $^2P_{1/2}$ ground states in $LaPO_4$ and $LuPO_4$. In ref.[31], we reported the VRBE diagrams of ARE(Si,Ge)O_4 (A = Li, Na; RE = Y, Lu) family compounds. The real VRBE in the Bi^{2+} $^2P_{1/2}$ ground states still remained unclear. The study on VRBE in the Bi^{2+} level locations will help to unravel the charge carrier trapping processes and the rational design of new Bi^{3+} doped afterglow phosphors.

We have studied in ref. [31] the AREGeO_4 (A = Li, Na; RE = Y, Lu) solid solution family of compounds doped with Bi^{3+}, Eu^{3+}, Tb^{3+}, and Pr^{3+} doping. That study resulted in the VRBE scheme of Fig. 1 that was also published in ref.[31]. The combination Bi^{3+}-Eu^{3+} was also studied in ref.[31]. The new content in this work is that the combination Bi^{3+}-Nd^{3+}, Bi^{3+}-Tb^{3+}, and Bi^{3+}-Pr^{3+} in $NaYGeO_4$ and the combination Bi^{3+}-Tb^{3+} in $NaLu_{1-x}Y_xGeO_4$ solid solutions was studied to explore afterglow phosphors after exposure to X-rays and 254 nm UV-light for anti-counterfeiting and X-ray imaging applications. The thermoluminescence (TL) glow curves of Bi^{3+} and Bi^{3+}-Eu^{3+} codoped $NaYGeO_4$ were measured after charging by beta or gamma irradiation in ref. [31]. For X-ray imaging application, X-rays need to be used as the charging light source and the thermoluminescence properties of Bi^{3+} and/or lanthanide(s) doped $NaYGeO_4$ after X-ray charging is still unknown. Recently, Ou *et al.* reported $NaLuF_4$:Tb(15 mol%)@$NaYF_4$ nanocrystals for 3D X-ray imaging applications in ref.[1]. About 30 days Tb^{3+} afterglow can be measurable in $NaLuF_4$:Tb(15 mol%)@$NaYF_4$ after exposure to X-rays. We obtained the optimized $NaLuF_4$:Tb(15 mol%)@$NaYF_4$ nanocrystals produced by the authors from ref. [1]. To evaluate the X-rays induced afterglow performance in bismuth and/or lanthanides doped $NaYGeO_4$, in this work we will compare the TL intensities of bismuth and/or lanthanides doped $NaYGeO_4$ to that of $NaLuF_4$:Tb(15 mol%)@$NaYF_4$ nanocrystals after X-ray charging. Xu *et al.* reported good lanthanide and/or Cr^{3+} doped transparent (Y, Ga)$_3Al_2Ga_3O_{12}$ garnet afterglow ceramics after UV-light charging[32–34]. We obtained these optimized afterglow garnet ceramics from Dr. Jian Xu. We will compare the afterglow intensities of bismuth and/or lanthanides doped $NaYGeO_4$ developed in this work after 254 nm UV-light charging to that of lanthanide and/or Cr^{3+} doped transparent (Y, Ga)$_3Al_2Ga_3O_{12}$ garnet afterglow ceramics produced by Dr. Xu in refs.[33,34].

Fig. 1(a) predicts that, like Bi^{3+}, Tb^{3+} and Pr^{3+} can also act as hole capturing centres in $NaYGeO_4$. One then can further verify the Bi^{2+} $^2P_{1/2}$ ground state location by studying the thermoluminescence properties of Bi^{3+} and/or Ln^{3+} co-doped $NaYGeO_4$. Assuming that there is an electron de-trapping process from Bi^{2+}, recombination of the electron from Bi^{2+} with holes trapped at Bi^{4+}, Tb^{4+}, or Pr^{4+} should lead to a same TL glow curve but with characteristic emission from Bi^{3+}, Tb^{3+}, or Pr^{3+}. In this work, we will evidence the electron liberation process from Bi^{2+} by

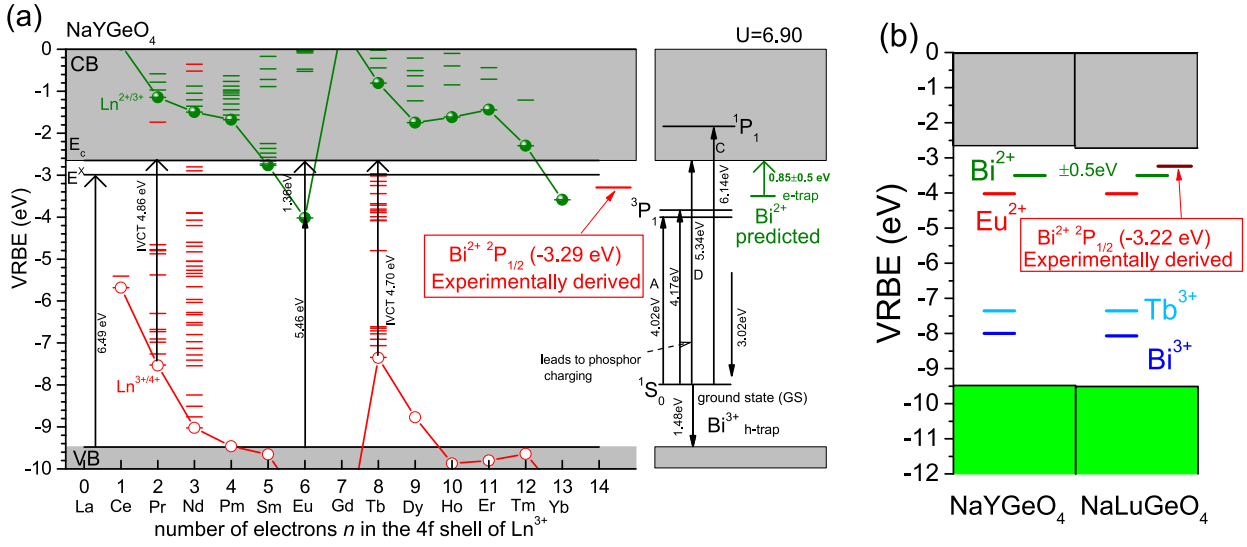

Fig. 1. (a) Vacuum referred binding energy (VRBE) diagram for $NaYGeO_4$ compound with the Tb^{3+}, Pr^{3+}, Nd^{3+}, Bi^{3+}, and Bi^{2+} energy level locations. (b) Stacked VRBE diagram for $NaYGeO_4$ and $NaLuGeO_4$.

deeply studying the Bi^{3+} and/or lanthanides doped $NaYGeO_4$. Results show that Bi^{3+} can act as a shallow electron trap, while Bi^{3+}, Tb^{3+}, and Pr^{3+} act as deep hole trapping and recombination centres in $NaYGeO_4$. The trap depth of Bi^{3+} electron trapping centre is found to be about 0.64 eV by thermoluminescence study. The VRBE in the Bi^{2+} $^2P_{1/2}$ ground state is then determined to −3.29 eV in $NaYGeO_4$. The electron trap depth produced by the Bi^{3+} codopant in $NaLu_{1-x}Y_xGeO_4$:0.003Bi^{3+},0.008Tb^{3+} solid solutions can be adjusted, by increasing x, resulting in conduction band engineering.

High X-ray storage capacity phosphors were developed in the optimized $NaYGeO_4$:0.004Bi^{3+} and $NaYGeO_4$:0.003Bi^{3+},0.008Tb^{3+} by using Bi^{3+} as an electron trap and Bi^{3+} and Tb^{3+} as the hole trapping centres. The integrated TL intensity after X-ray charging for $NaYGeO_4$:0.004Bi^{3+} is about 4.5 and 2.3 times higher than that of the state-of-the-art storage phosphor BaFBr(I):Eu^{2+} and the optimized $NaLuF_4$:Tb^{3+} afterglow phosphor in ref. [1]. The integrated TL intensity after X-ray charging for $NaYGeO_4$:0.003Bi^{3+},0.008Tb^{3+} is about 1.1, 1.1, and 1.9 times higher than that of the state-of-the-art BaFBr(I):Eu^{2+}, $SrAl_2O_4$:Eu^{2+},Dy^{3+}, and the optimized $NaLuF_4$:Tb^{3+} in ref. [1]. Particularly, the optimized $NaYGeO_4$:0.003Bi^{3+},0.008Tb^{3+} after 254 nm UV-light charging shows good initial afterglow intensity, which is higher than that of the optimized YAGG:Tb^{3+},Cr^{3+} transparent afterglow ceramic in the first ~ 10 s. We will show proof-of-concept color tailoring for anti-counterfeiting applications by combining perovskite $CsPbI_3$ quantum dots (QD) with finely designed charge carriers in $NaYGeO_4$ where Bi^{3+} acts as an electron trap while both Tb^{3+} and Pr^{3+} act as the hole trapping and recombination centres. Proof-of-concept X-ray storage application was demonstrated in the optimized $NaYGeO_4$:0.004Bi^{3+} and $NaYGeO_4$:0.003Bi^{3+},0.008Tb^{3+} phosphors and silicon gel based flexible X-ray imaging films.

2. Experimental

All starting chemicals were purchased from Shanghai Aladdin chemical company and utilized without further treatment. The phosphor compounds were prepared via a typical conventional high temperature solid state reaction method. The appropriate stoichiometric mixture of Bi_2O_3 (99.99%), Na_2CO_3 (99.99%), Y_2O_3 (99.99%), Lu_2O_3 (99.99%), GeO_2 (99.99%), and rare earth oxides with high purity of 4 N (99.99%) was ground and mixed for ~ 15 min in agate mortar with the help of acetone. Then, the mixture was carefully placed in a covered alumina crucible and heated at 1200 °C for 6 h in a tube furnace under ambient atmosphere. The used heating rate for the furnace is 5 °C/min. Finally, the synthesized compounds were cooled to room temperature (RT) and ground and milled well before further measurements. The afterglow properties of $NaYGeO_4$:0.004Bi^{3+} and $NaYGeO_4$:0.003Bi^{3+}, 0.008 Tb^{3+} have been optimized by adjusting synthesis temperature and the concentration of dopants.

To compare afterglow performance of the optimized $NaYGeO_4$: 0.003Bi^{3+},0.008 Tb^{3+}, lanthanide and/or Cr^{3+} doped transparent garnet afterglow ceramics were synthesized by a high temperature solid state reaction in vacuum[33]. The detailed ceramic compositions are $(Gd_{0.995}Ce_{0.005})_3Al_{1.9995}Ga_3O_{12}$:0.0005$Cr^{3+}$ (GAGG:Ce^{3+},Cr^{3+}), $(Y_{0.995}Ce_{0.005})_3Al_{1.999}Ga_3O_{12}$: 0.001Cr (YAGG:$Ce^{3+}$,$Cr^{3+}$), $Y_{2.97}Al_{1.999}Ga_3O_{12}$:0.03$Tb^{3+}$,0.001$Cr^{3+}$ (YAGG:Tb^{3+},Cr^{3+}), $Y_{2.985}Al_{1.999}Ga_3O_{12}$:0.015$Pr^{3+}$,0.001$Cr^{3+}$ (YAGG:Pr^{3+},Cr^{3+}), and $Gd_{2.999}Ga_{4.9995}O_{12}$: 0.0005$Cr^{3+}$, 0.001$Eu^{3+}$ (GGG:Cr^{3+},Eu^{3+}) [35]. The above afterglow ceramics are produced by Dr. Xu in refs.[33,34] and are optimized samples that show intense afterglow after exposure to UV-light. To explore anti-counterfeiting application, $CsPbI_3$ quantum dot (QDs) was synthesized via a typical low-temperature solution reaction method[36,37]. Afterglow phosphors dispersed in flexible silicone films were explored to further demonstrate anti-counterfeiting application. The appropriate phosphors like $NaYGeO_4$:0.003Bi^{3+},0.008 Tb^{3+} were first sifted by 200 mesh sieve and then were added into silicon gel (Sylgard 184, Dow Corning) and mixed well to generate a film on a smooth glass substrate. Then, the film was placed at 60 °C in vacuum for 4 h.

The crystal structures of synthesized compounds were checked using a Rigaku Smar/SmartLa X-ray diffraction system equipped with Cu Kα (λ = 0.15405 nm) X-ray tube at 40 kV and 30 mA. The scanning electron microscope (SEM) photographs and energy dispersive X-ray spectroscopy (EDX) mapping were recorded by a JEOL JSM-7610FPlus scanning electron microscope. Photoluminescence emission (PL), PL excitation (PLE) spectra, afterglow spectra, and room temperature (RT) *iso*-thermal decay curves were measured using a FLS920 spectrometer (Edinburgh), which contains a 450 W Xe900 continuous xenon lamp, a monochromator, and a single photon counting photomultiplier (Hamamatsu, R928P). The red-sensitive R928P photomultiplier works at −20 °C and has high quantum efficiency from 200 nm to 870 nm. The PL and PLE spectra are corrected by the wavelength-dependent excitation intensity of the xenon arc lamp.

Low-temperature thermoluminescence (LTTL) measurements between 100 K and 600 K and above RT thermoluminescence (TL) measurements were recorded by a facility that contains a thermostat, a R928P photomultiplier, a UV/vis spectrometer (Ocean Optics, model QE65Pro), a Hg lamp (254 nm), and a X-ray tube. Prior to all the LTTL and TL measurements, the samples were heated to 723 K for 5 mins to empty all trapped charge carriers and then cooled to initial temperature at 100 K for LTTL recording or at 300 K for above RT TL recording. For the LTTL measurements, phosphor powders were pressed into a pill and placed on the heater of the thermostat using silver paint in vacuum. For the 3D TL emission (TLEM) plot, the thermally stimulated emission was recorded by a QE65Pro detector. For optically stimulated luminescence measurements, the excitation light sources of daylight, 850 nm laser, 656 nm laser, 396 nm LED, 365 nm UV light, and white LED (WLED) are used. A sample is first charged by X-ray or 254 nm UV-light and then illuminated by different light stimulation with different duration time, and then a TL glow curve is recorded.

To study charge carrier trapping processes, thermoluminescence excitation (TLE) spectra were measured employing the FLS920 spectrometer (Edinburgh). Different energy photon with the wavelength from 200 nm to 300 nm was used to charge the Bi^{3+} and/or lanthanides doped $NaYGeO_4$ afterglow phosphors for a duration of 60 s and then RT *iso*-thermal decay curves were recorded for 60 s by monitoring the wavelength at 549 nm for Tb^{3+} emission and at 402 nm for Bi^{3+} emission. For the TLE measurements we recorded the afterglow decay for a duration of 60 s because the afterglow intensities are relatively intense during the first 60 s after switching off the excitation light. Integrated RT *iso*-thermal decay intensity for 60 s was corrected by the wavelength-dependent excitation intensity of the xenon arc lamp. A so-called TL excitation (TLE) plot like in Fig. 9 (b) is constructed by displaying the corrected *iso*-thermal decay intensity as a function of charging wavelength.

3. Results

3.1. X-ray diffraction and photoluminescence spectroscopy

High purity compounds are required for studying the charge carrier trapping processes. We therefore measured the X-ray diffraction patterns (XRD) for the as-synthesized Bi^{3+} and/or lanthanide doped $NaYGeO_4$, which are shown in Fig. 2(a). All prepared samples have single phase and their XRD patterns match well with $NaYGeO_4$ reference card (No. PDF#88–1177). The dopants are assumed to substitute the Y^{3+} sites in the crystal. One expects a slight shift of the XRD pattern near 32° towards a lower angle after Bi^{3+} and/or lanthanides codoping since the radius of Y^{3+} (r = 0.9 Å, CN = 6) is smaller than that of Bi^{3+} (r = 1.03 Å, CN = 6), Tb^{3+} (r = 0.92 Å, CN = 6), and Nd^{3+} (r = 0.98 Å, CN = 6). Compared with the XRD pattern of $NaYGeO_4$ host, Fig. 2(b) shows that this expected shift does not appear. Possibly the concentration of doped bismuth and lanthanides is too low and then the increase of cell volume of $NaYGeO_4$ is too small.

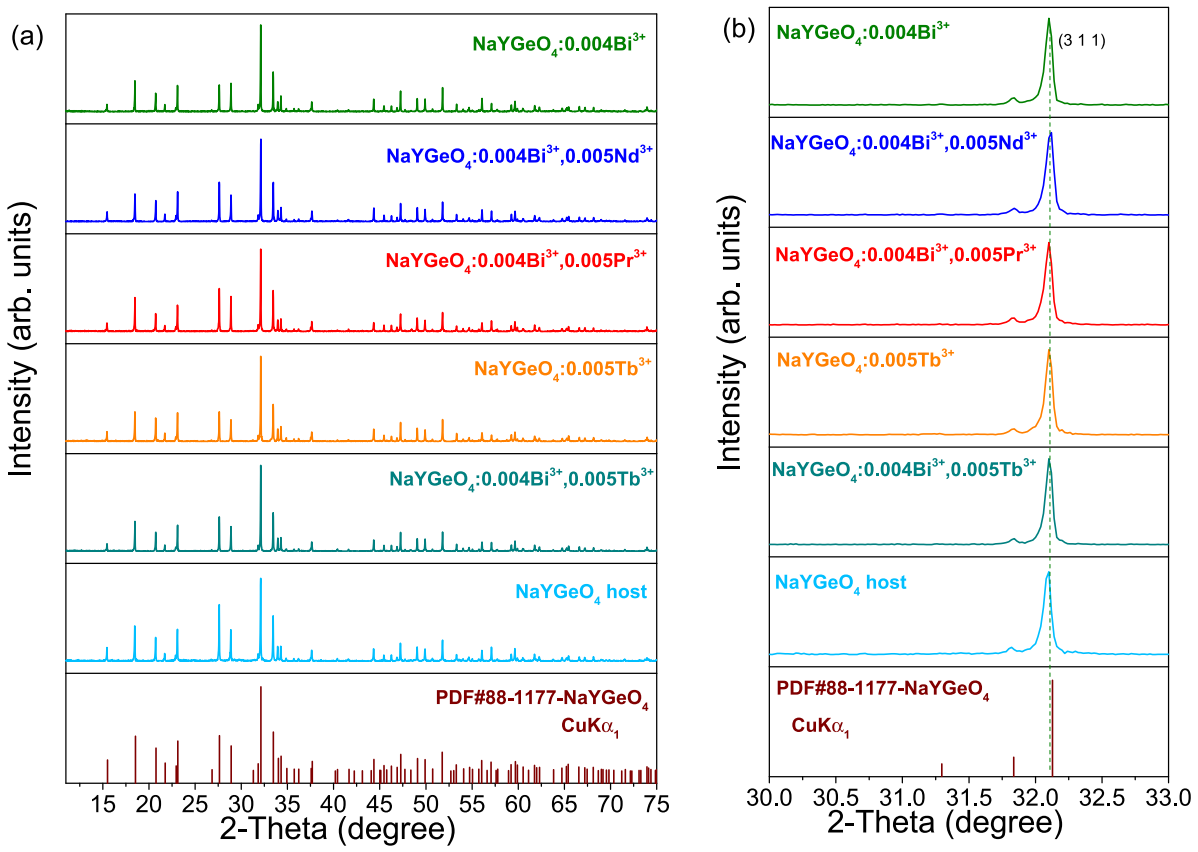

Fig. 2. (a) XRD patterns for the as-synthesized compounds of Bi^{3+} and/or lanthanide doped $NaYGeO_4$ and $NaYGeO_4$ host. (b) Detailed XRD patterns in the range from 30° to 33°.

In order to understand the complex charge carrier trapping processes in bismuth and/or lanthanides doped $NaYGeO_4$, we need to first know the fundamental luminescence properties of bismuth and/or lanthanides doped $NaYGeO_4$. We therefore first measured the photoluminescence excitation spectra, emission spectra, and afterglow spectra for the bismuth and/or lanthanides doped $NaYGeO_4$ which are shown in Fig. 3. Fig. 3(a) shows the PLE and PL spectra of $NaYGeO_4$:0.004Bi^{3+}. A similar spectrum recorded at 10 K and extending to the vacuum ultra violet range was published in ref.[31]. Characteristic Bi^{3+} D-band excitation near 238 nm and Bi^{3+} A-bands near 298 nm and 310 nm due to Jahn-Teller splitting of the Bi^{3+} $^3P_1$ excited state appear as observed previously in ref.[31]. Fig. 3 in ref. [38] shows that the band at 43000 cm^{-1} is not from an intrinsic Bi^{3+} excitation which confirms the assignment as D-band in $NaLuGeO_4$ and $NaYGeO_4$. Upon 298 nm excitation, $NaYGeO_4$:0.004Bi^{3+} shows a broad emission band peaked at about 402 nm, which is due to the Bi^{3+} $^3P_1 \rightarrow {}^1S_0$ transition (A-band), see also ref. [31]. Charged by Bi^{3+} D-band excitation with a Hg lamp, Bi^{3+} $^3P_1 \rightarrow {}^1S_0$ blue afterglow emerges in Fig. 3(b). After co-doping Nd^{3+} into $NaYGeO_4$:0.004Bi^{3+}, similar PLE and PL spectra appear in Fig. 3(c) as in Fig. 3(a). Fig. 3 (d) shows the RT *iso*-thermal decay curves of $NaYGeO_4$:0.004Bi^{3+},0.005Nd^{3+} after Hg lamp charging. In addition to the Bi^{3+} afterglow as observed in $NaYGeO_4$:0.004Bi^{3+} in Fig. 3(b), new Nd^{3+} 1062 nm infrared persistent luminescence appears in $NaYGeO_4$:0.004Bi^{3+},0.005Nd^{3+} in Fig. 3(d).

Fig. 3(e) and Fig. S3 shows the PLE and PL spectra for $NaYGeO_4$:0.005Tb^{3+}. Like in ref.[31], the PLE peaks near 248 and 286 nm are assigned to Tb^{3+} 4f → 5d transitions, while the fitted PLE peak near 262 nm is assigned to the Intervalence Charge Transfer Band (IVCT), which is induced by electron transfer from the Tb^{3+} 4f ground state to the conduction band (CB), i.e., Tb^{3+}→CB IVCT. In ref.[31] an excitation band peaked near 236 nm was observed in the excitation spectrum of $NaYGeO_4$:0.01Tb^{3+} in Fig. S5(h). It is absent in Fig. 3(e). The observed 236 nm excitation band in ref. [31] could be due to host-related defect(s). After exposure to 254 nm UV-light, during more than 25 min typical Tb^{3+} 4f → 4f afterglow appears in Fig. 3 (f) and Fig. S4.

Fig. 3(g) shows the PLE and PL spectra of $NaYGeO_4$:0.003Bi^{3+},0.008Tb^{3+}. Upon 254 nm excitation, the emission spectrum is mainly composed of characteristic Tb^{3+} 4f-4f transitions. Monitored at the Tb^{3+} 549 nm typical emission, not only Tb^{3+} 4f → 5d excitation band peaked near 253 nm and Tb^{3+}→CB IVCT band peaked near 260 nm but also Bi^{3+} excitation A-band appear in the excitation spectrum. It suggests that there is an energy transfer process from Bi^{3+} to Tb^{3+}. Compared with $NaYGeO_4$:0.005Tb^{3+} in Fig. 3(f), about 10 times stronger Tb^{3+} afterglow emerges in the Bi^{3+},Tb^{3+}-codoped $NaYGeO_4$:0.003Bi^{3+},0.008Tb^{3+} in Fig. 3(h) and 3(i). Fig. 3(j) further demonstrates that the Tb^{3+} afterglow at 549 nm is much stronger than the 402 nm afterglow in $NaYGeO_4$:0.003Bi^{3+},0.008Tb^{3+}.

3.2. *Evidencing the electron liberation process from Bi^{2+}*

To understand the afterglow observed in Fig. 3 and to discuss the charge carrier trapping and de-trapping processes in bismuth and/or lanthanides doped $NaYGeO_4$, low-temperature thermoluminescence emission (TLEM) spectra were recorded after exposure to X-rays at 100 K. Fig. 4(a) shows the TLEM plot for $NaYGeO_4$:0.005Tb^{3+}. TL glow peaks near 161, 219, and 284 K with characteristic Tb^{3+} 4f → 4f emission appear in $NaYGeO_4$:0.005Tb^{3+}. Fig. 4(b) shows the TLEM plot for $NaYGeO_4$:0.004Bi^{3+}. A strong TL glow peak near 270 K with characteristic Bi^{3+} A-band emission emerges in $NaYGeO_4$:0.004Bi^{3+}. Particularly, a similar TL glow peak near 272 K appears in $NaYGeO_4$:0.004Bi^{3+},0.005Tb^{3+} in Fig. 4(c) and in $NaYGeO_4$:0.004Bi^{3+},0.005Pr^{3+} in Fig. 4(d) where the thermally stimulated emission is from Tb^{3+} or Pr^{3+} typical 4f → 4f emission rather than Bi^{3+} A-band emission. The TL glow peak near ~ 270 K is absent in $NaYGeO_4$:0.005Tb^{3+} in Fig. 4(a) but

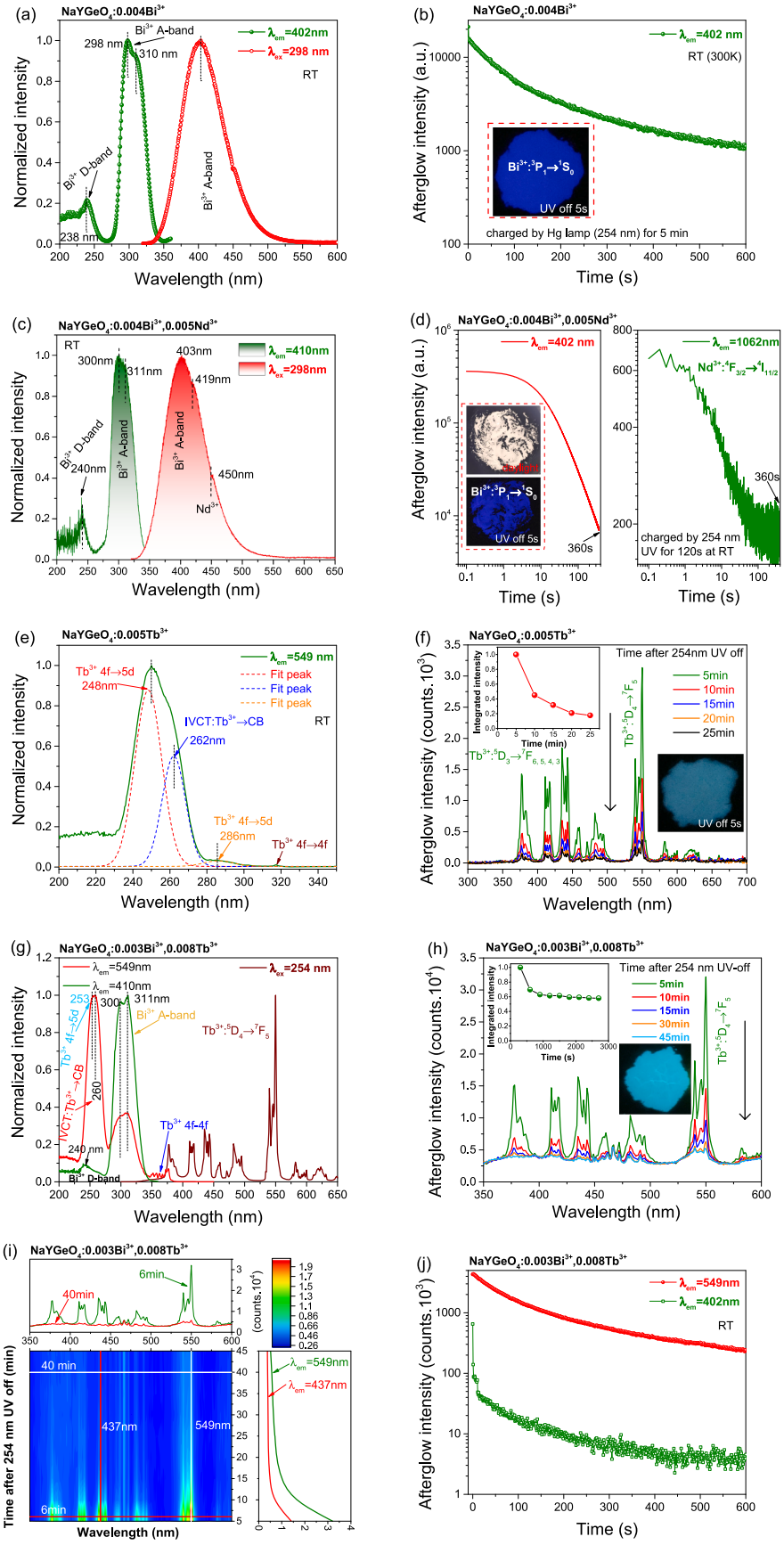

Fig. 3. Photoluminescence excitation (PLE) and emission (PL) spectra, RT *iso*-thermal decay curve and afterglow spectra as a function of time after exposure to 5 min 254 nm UV-light charging for (a)-(b) $NaYGeO_4$:0.004Bi^{3+}, (c)-(d) $NaYGeO_4$:0.004Bi^{3+},0.005Nd^{3+}, (e)-(f) $NaYGeO_4$:0.005Tb^{3+}, and (g)-(j) the optimized afterglow phosphor $NaYGeO_4$:0.003Bi^{3+},0.008 Tb^{3+}. The insets in (b), (d), (f), and (h) are the afterglow photographs after 254 nm UV-light illumination in the dark.

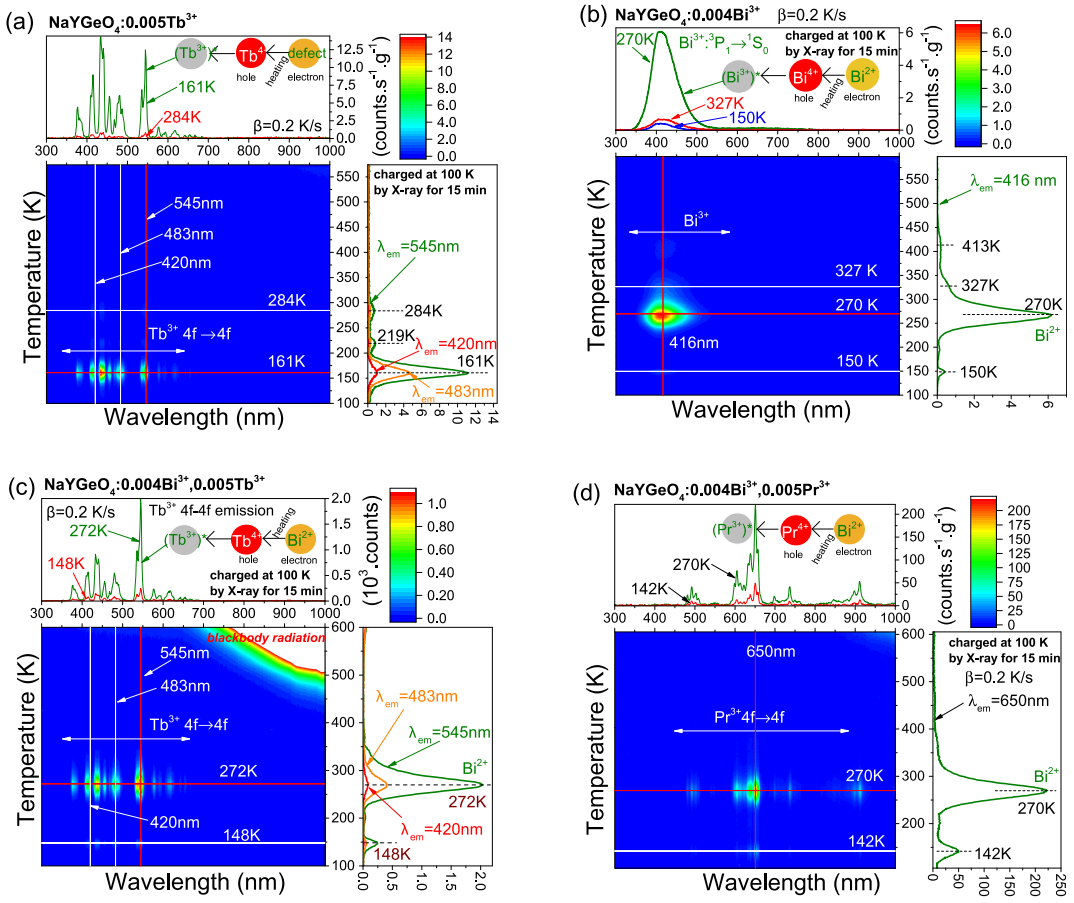

Fig. 4. Low-temperature thermoluminescence (TL) emission spectra for (a) $NaYGeO_4$:0.005Tb^{3+}, (b) $NaYGeO_4$:0.004Bi^{3+}, (c) $NaYGeO_4$:0.004Bi^{3+},0.005Tb^{3+}, and (d) $NaYGeO_4$:0.004Bi^{3+},0.005Pr^{3+} after exposure to X-ray charging at 100 K. The used heating rate is 0.2 K/s in (a)-(d).

emerges in Fig. 4(b)-(d) when Bi^{3+} is present in $NaYGeO_4$. We will attribute the 270 K TL glow peak to electron liberation from Bi^{2+} and recombination with holes at Bi^{4+} in Fig. 4(b), at Tb^{4+} in Fig. 4 (c), and at Pr^{4+} in Fig. 4(d) to generate characteristic Bi^{3+} $^3P_1 \rightarrow {}^1S_0$ emission and Tb^{3+} and Pr^{3+} 4f → 4f emissions.

In ref. [31] both the VRBE diagrams of $NaYGeO_4$ and $NaLuGeO_4$ have been presented. The VRBE at the conduction band bottom of $NaLuGeO_4$ is about 0.1 eV lower than that of $NaYGeO_4$. Assuming that the VRBEs at the Bi^{2+} and Eu^{2+} ground state level locations remain stationary, one expects that the electron trap depths of Bi^{3+} and Eu^{3+} will increase in $NaLu_{1-x}Y_xGeO_4$ solid solutions with increasing x. This prediction has been verified in $NaLu_{1-x}Y_xGeO_4$:0.01Bi^{3+},0.001Eu^{3+} and in $NaLu_{1-x}Y_xGeO_4$:0.01Bi^{3+} that has been published in ref.[31]. Fig. 5(a) reproduces the low-temperature TL glow curves for $NaLu_{1-x}Y_xGeO_4$:0.01Bi^{3+} after beta irradiation. Fig. 1 predicts that Bi^{3+} can act as an electron trap, while Tb^{3+} can act as a hole trapping and recombination centre. Therefore, we made $NaLu_{1-x}Y_xGeO_4$:0.003Bi^{3+},0.008Tb^{3+} solid solutions to demonstrate the electron liberation from Bi^{2+} and to explore Tb^{3+} afterglow phosphors for anti-counterfeiting and X-ray imaging applications. Fig. 5(b) and S6(a) show the normalized and unnormalized low-temperature thermoluminescence glow curves for $NaLu_{1-x}Y_xGeO_4$:0.003Bi^{3+},0.008Tb^{3+} solid solutions after exposure to X-rays at 93 K. Like in Fig. 5(a), the TL glow peak named Bi^{2+} peak gradually shifts from ~ 233 K for x = 0 to ~ 283 K for x = 1 with increasing x in $NaLu_{1-x}Y_xGeO_4$:0.003Bi^{3+},0.008Tb^{3+}. This TL glow peak shifting will be assigned to the increased electron trap depth of Bi^{3+} when increasing x in $NaLu_{1-x}Y_xGeO_4$:0.003Bi^{3+},0.008Tb^{3+}. Table 1 lists the TL results and calculated electron trapping depths for the Bi^{2+} TL glow peaks for $NaLu_{1-x}Y_xGeO_4$:0.003Bi^{3+},0.008Tb^{3+} based on a first-order TL recombination kinetics and assuming zero distribution in Bi^{2+} trap depth. The reported Bi^{2+} trapping depths and the frequency factors for $NaLu_{1-x}Y_xGeO_4$:0.003Bi^{3+},0.008Tb^{3+} then should be treated as indicative. Assuming a typical fixed frequency factor of 1×10^{13} s^{-1} for $NaLu_{1-x}Y_xGeO_4$[23], the Bi^{2+} trapping depth in $NaLu_{1-x}Y_xGeO_4$:0.003Bi^{3+},0.008Tb^{3+} can be determined by a first-order TL recombination kinetics to 0.64, 0.68, 0.71, 0.75, and 0.78 eV for x = 0–1. These values are larger than that in column 4 of Table 1 because a larger frequency factor of 1×10^{13} s^{-1} is used.

We know from combining experimental results with empirical models that the Bi^{2+} ground state level should be located around −3.5 +/- 0.5 eV in inorganic compounds as also indicated for $NaYGeO_4$ in the scheme of Fig. 1. Similarly we know from Lyu and Dorenbos (T. Lyu, P. Dorenbos, Chem. Mater. 32 (2020) 1192.)[31] that compounds like $LiLuSiO_4$, $LiYSiO_4$, $LiLuGeO_4$, and $LiYGeO_4$ all have the VB-top near −9.5 eV. One can combine that knowledge with studies by Qiao et al. (Zheng Qiao, Xuesong Wang, Chen Heng, Wei Jin, Lixin Ning, Inorg. Chem. 60 (2021) 16604.)[39] in 2021 on $LiREGeO_4$ (RE = Sc, Y, Lu) where the Bi^{2+} ground state is computed about 6 eV above the VB-top. This brings the Bi^{2+} ground state indeed near −3.5 eV. One, if not the first, direct computation of the VRBE in the Bi^{2+} ground state was by Lou et al. (Bibo Lou, Jun Wen, Lixin Ning, Min Yin, Chong-Geng Ma, Chang-Kui Duan, Phys. Rev. B 104 (2021) 115101)[40]. In the $REAlO_3$ (RE = La, Gd, Y), $LaGaO_3$, and $LaInO_3$ perovskites the Bi^{2+} ground state is always computed near −4 eV. Considering the above, we do expect Bi^{3+} to act as a 0.85 +/-0.5 eV deep electron trap in $NaYGeO_4$. The observation of an intense glow peak near ~ 272 K at β = 0.2 K/s in Fig. 4 and near 283 K at β = 1 K/s in Fig. 5(b) due to an electron releasing trapping center, strongly suggests that this peak is due to electron release from Bi^{2+} when Bi^{3+} is present in the compound.

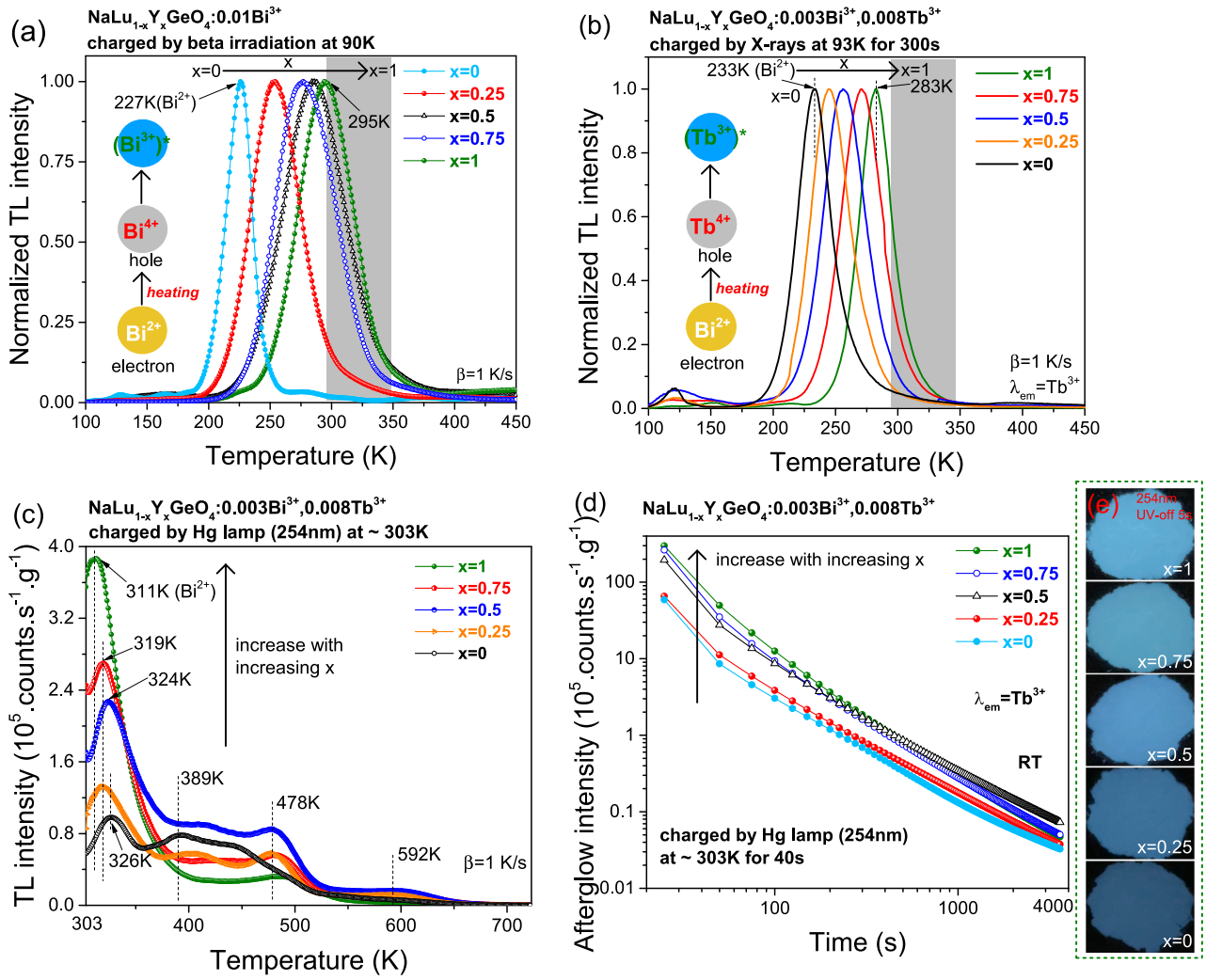

Fig. 5. TL glow curves for (a) $NaLu_{1-x}Y_xGeO_4$:0.01Bi^{3+} after beta irradiation and (b)-(c) $NaLu_{1-x}Y_xGeO_4$:0.003Bi^{3+},0.008Tb^{3+} after X-rays or 254 nm UV-light charging measured at β = 1 K/s. (d) RT isothermal decay curves and (e) afterglow photographs for $NaLu_{1-x}Y_xGeO_4$:0.003Bi^{3+},0.008Tb^{3+} after exposure to 254 nm UV-light. The Tb^{3+} emission was monitored and the afterglow was corrected by sample mass and irradiation time. The data in (a) was reproduced from ref.[31]. The Bi^{3+} emission was monitored in (a) and the Tb^{3+} emissions were monitored in (b).

Table 1
TL results for $NaLu_{1-x}Y_xGeO_4$:0.003Bi^{3+},0.008Tb^{3+} providing the frequency factor s (s^{-1}) and the electron trap depths E (eV) for the Bi^{2+} glow peaks (T_m). The frequency factors for x = 0–0.75 were obtained from ref. [31] and the frequency factor for x = 1 was obtained from this work.

x	s	T_m Bi^{2+} (K)	Bi E (eV)
0	9.23×10^9	233	0.50
0.25	3.73×10^9	245	0.51
0.50	3.16×10^9	256	0.54
0.75	9.73×10^9	271	0.59
1	1.23×10^{10}	283	0.63

To evaluate afterglow properties, we also measured above RT TL glow curves for $NaLu_{1-x}Y_xGeO_4$:0.003Bi^{3+},0.008Tb^{3+} after 254 nm UV-light charging as shown in Fig. 5(c) and after X-ray charging for x = 1 in Fig. S6(b). Fig. 5(c) shows that the TL glow peak near 311 K appears to shift towards a higher temperature and the TL intensity decreases with decreasing x. This is because that the RT TL glow curves in Fig. 5(c) are in the tail of the glow peak that shifts from ~ 233 K to ~ 283 K in Fig. 5 (b) and there is a distribution in Bi^{2+} trapping depths in $NaLu_{1-x}Y_xGeO_4$:0.003Bi^{3+},0.008Tb^{3+}. With the above RT TL glow curves in Fig. 5(c) then only the deepest Bi^{2+} traps contribute to the 311 K TL glow peak.

To study the Bi^{2+} trap distribution, we used the peak cleaning technique for x = 1 sample ($NaYGeO_4$:0.003Bi^{3+},0.008 Tb^{3+})[19,41]. After exposure to 254 nm UV-light for a duration of 20 s at RT, the x = 1 sample was rapidly heated at a heating rate of 5 K/s to the peak clean temperature (T_{clean}) and maintained at that T_{clean} for 60 s. The sample was then cooled to RT and a TL glow curve was recorded at a heating rate of 1 K/s. Fig. S6(c) demonstrates that the TL glow peak near RT shifted towards a higher temperature and the TL intensity decreased with increasing T_{clean}. This indicates that there is a trap depth distribution for the sample with x = 1, and the increase in TL glow peak is because of the fact that the electrons captured in the shallow Bi^{2+} traps have been released at T_{clean} and only the electrons at deeper Bi^{2+} traps remain occupied. Fig. S6(b) compares the TL glow curves of the x = 1 sample charged with X-rays and 254 nm UV-light with a same heating rate of 1 K/s. The TL glow peak shifts from ~ 311 K to ~ 340 K when the charging is changed from 254 nm UV-light to X-rays. Apparently, stable and deeper Bi^{2+} traps capture more efficiently free charge carriers during X-ray exposure and then higher TL glow peak (T_m) appears upon X-ray charging. Another possible reason is that with optical excitation the liberated electron is trapped relatively close to the hole trapping center. The electron does not need to go through the CB in order to recombine with the hole. Effectively this will lower the energy barrier

for detrapping and thus a lower temperature glow peak. With X-ray excitation seperate hole trap and electron trap are created and recombination is realized via the CB. The same applies for $NaYGeO_4$:yBi^{3+},0.008 Tb^{3+} (y = 0.001–0.012) as shown in Fig. S13(b)-S13(c) and the lanthanide and/or bismuth doped $NaYGeO_4$ in Fig. 7 (b) and 7(c).

Fig. 5 (d)-(e) shows the RT isothermal decay curves and afterglow photographs for $NaLu_{1-x}Y_xGeO_4$:0.003Bi^{3+},0.008 Tb^{3+} after exposure to 254 nm UV-light. The Tb^{3+} afterglow increases with increasing x in $NaLu_{1-x}Y_xGeO_4$:0.003Bi^{3+},0.008 Tb^{3+}.

3.3. *Designing afterglow phosphor by using electron release from Bi^{2+}*

To unravel the nature of the recombination centres and to design afterglow phosphors, we measured above RT TL emission (TLEM) spectra for the bismuth and/or lanthanide(s) doped $NaYGeO_4$ as shown in Fig. 6. TL glow peaks near 340, 451 and 579 K with typical Tb^{3+} 4f → 4f emission appear in $NaYGeO_4$:0.005Tb^{3+} in Fig. 6(a). For $NaYGeO_4$:0.004Bi^{3+} in Fig. 6(b), TL glow peaks near 335 K and 418 K with characteristic Bi^{3+} A-band emission emerge. TL glow peaks near 373 K and 446 K were observed in $NaYGeO_4$:0.01Bi^{3+} in Fig. 6 (a) in ref. [31] where there was about 20 min time between γ-ray charging and the start of the TL-readout. It means that the stored charge carriers in the shallower traps are already de-trapped before TL-readout and the 335 K TL glow peak near RT will shift towards a higher temperature 373 K. The 418 and 446 K TL glow peaks are assigned to electron liberation from different host-related intrinsic defects in $NaYGeO_4$ and recombination with holes captured at Bi^{4+}. Compared with $NaYGeO_4$:0.004Bi^{3+} in Fig. 6(b), similar TL glow peaks also appear in $NaYGeO_4$:0.004Bi^{3+},0.005Nd^{3+} in Fig. 6(c) where the recombination emission comes from both typical Bi^{3+} A-band and Nd^{3+} infrared 4f → 4f transitions. Fig. 6(d) shows the TLEM plot for the optimized $NaYGeO_4$:0.003Bi^{3+},0.008 Tb^{3+}. Strong TL glow peaks near 349 and 484 K with typical Tb^{3+} 4f-4f emission are observed with the TL intensity about 10 times higher than that of other compounds in Fig. 6(a)-(c).

To compare the charge carrier storage capacity properties of the prepared lanthanide and/or bismuth doped $NaYGeO_4$, X-ray excited emission as a function of time, TL glow curves after exposure to X-rays and 254 nm UV-light were measured and shown in Fig. 7 (a)-7(c). Fig. 7 (a) shows the X-ray excited emission intensities for bismuth and/or lanthanide(s) doped $NaYGeO_4$, commercial Al_2O_3:C single chip, $SrAl_2O_4$:Eu^{2+},Dy^{3+}, and BaFBr(I):Eu^{2+}, and the $NaLuF_4$:Tb^{3+} from ref. [1]. In this experiment we switched on the X-ray beam and continuously monitored all the emission intensity from the sample via a photomultiplier (PMT). A SCHOTT BG-39 filter from about 300 to 800 nm was placed between the PMT tube and the sample. The ratios of integrated X-ray excited emission intensities from 0 to 200 s of bismuth and/or lanthanide(s) doped $NaYGeO_4$, Al_2O_3:C, $SrAl_2O_4$:Eu^{2+},Dy^{3+}, and $NaLuF_4$:Tb^{3+} to that of BaFBr(I):Eu^{2+} are shown in the legend in Fig. 7 (a). The integrated X-ray excited emission intensity of $NaLuF_4$:Tb^{3+} from ref.[1] is higher than that of other lanthanide and/or bismuth doped $NaYGeO_4$. It means that more X-ray photons are converted into visible light. $NaYGeO_4$:0.004Bi^{3+} shows the strongest X-ray excited emission intensity among the bismuth and/or lanthanide(s) doped $NaYGeO_4$.

The afterglow phosphors were charged by both X-rays and 254 nm UV-light for X-ray imaging application. Fig. 7(b) shows the TL glow curves of bismuth and/or lanthanide(s) doped $NaYGeO_4$ after X-ray charging. The ratios of integrated TL intensities between 305 and 723 K

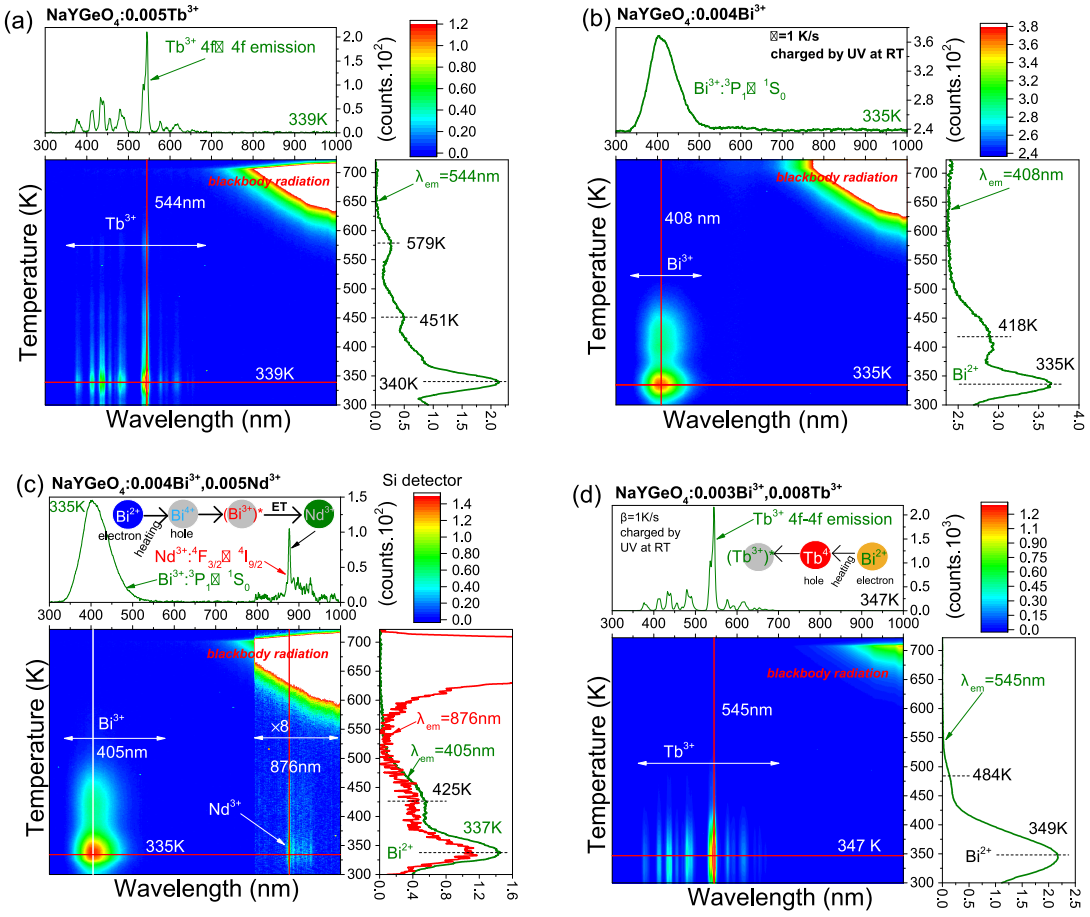

Fig. 6. Thermoluminescence (TL) emission plots for (a) $NaYGeO_4$:0.005Tb^{3+}, (b) $NaYGeO_4$:0.004Bi^{3+}, (c) $NaYGeO_4$:0.004Bi^{3+},0.005Nd^{3+}, and (d) $NaYGeO_4$:0.003Bi^{3+},0.008 Tb^{3+} after Hg lamp (254 nm) illumination for 5 min. The used heating rate is 1 K/s.

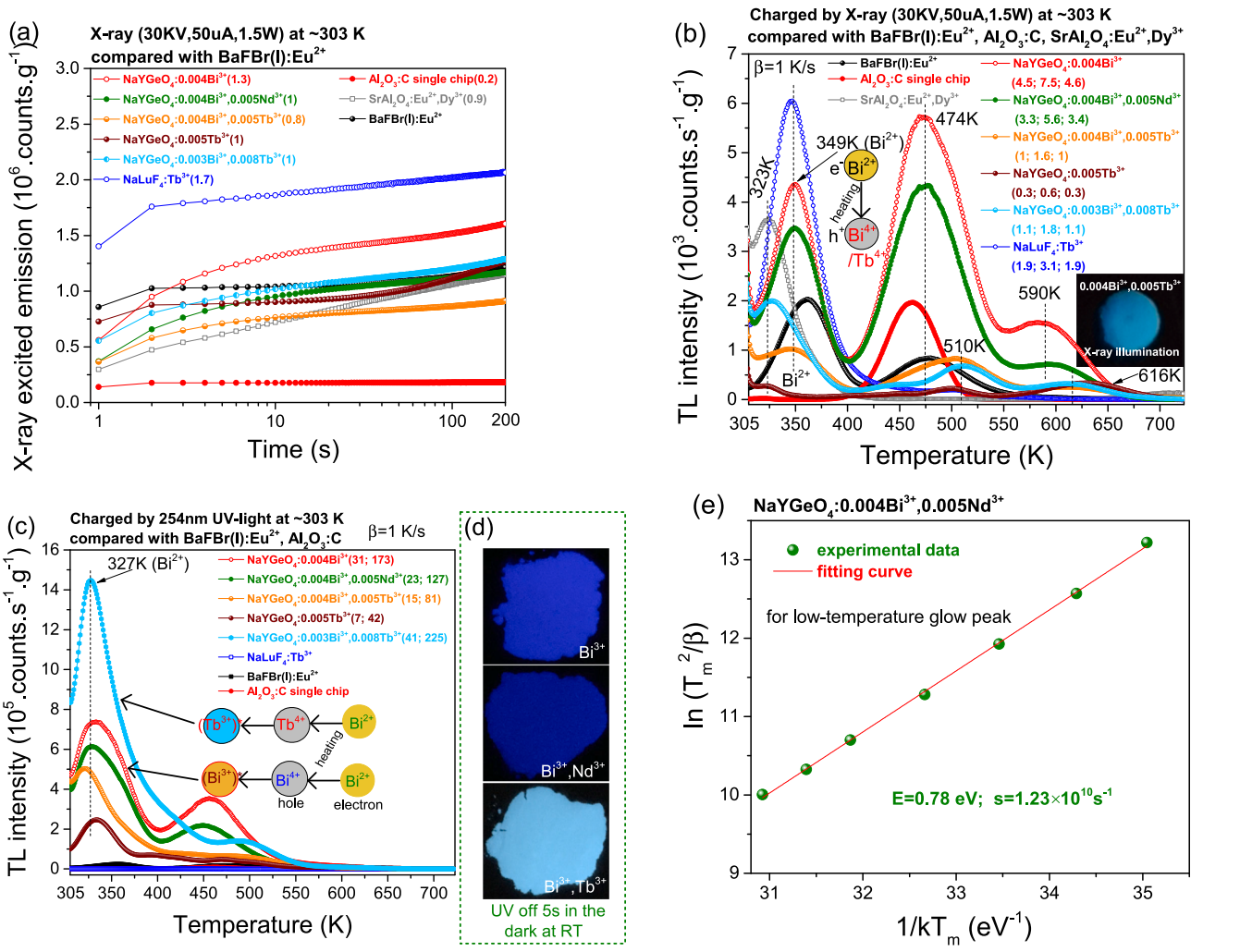

Fig. 7. (a) X-ray excited emission as a function of time, TL glow curves at β = 1 K/s for lanthanide and/or Bi^{3+} doped $NaYGeO_4$, $NaLuF_4$:Tb^{3+} from ref. [1], and the state-of-the-art BaFBr(I):Eu^{2+}, $SrAl_2O_4$:Eu^{2+},Dy^{3+}, and Al_2O_3:C single crystal chip after exposure to (b) 1.5 W X-rays and (c) 254 nm UV-light. (d) a comparison of afterglow photographs after UV-light charging. (e) variable heating rate plot for $NaYGeO_4$:0.004Bi^{3+},0.005Nd^{3+} after X-ray charging. The used heating rates were 0.2, 0.4, 0.8, 1.6, 3, 4.5, and 6.4 K/s.

of bismuth and/or lanthanide(s) doped $NaYGeO_4$ to that of BaFBr(I):Eu^{2+}, Al_2O_3:C, and $SrAl_2O_4$:Eu^{2+},Dy^{3+} are shown in the legend of Fig. 7(b). The TL intensity of $NaYGeO_4$:0.004Bi^{3+} and the optimized $NaYGeO_4$:0.003Bi^{3+},0.008 Tb^{3+} is about 4.5 and 1.1 times higher than that of the state-of-the-art BaFBr(I):Eu^{2+} after X-ray charging. Like in $NaYGeO_4$:0.01Bi^{3+} in Fig. 7(e) in ref.[31], the TL glow peak near 349 K in Bi^{3+}-codoped $NaYGeO_4$ in Fig. 7(b) will be assigned to electron release from Bi^{2+} and recombination with holes captured at Bi^{4+} and Tb^{4+} generating characteristic Bi^{3+} $^3P_1 \rightarrow {}^1S_0$ emission and Tb^{3+} 4f → 4f emissions. Other common TL glow peaks near 474, 510, and 590 K in Fig. 7(b) will be assigned to electron liberation from host-related intrinsic defect(s).

Fig. 7(c) shows the TL glow curves for bismuth and/or lanthanide(s) doped $NaYGeO_4$ after 254 nm UV-light charging. The ratios of the integrated intensities between 305 and 723 K of bismuth and/or lanthanide(s) doped $NaYGeO_4$ to that of BaFBr(I):Eu^{2+} and Al_2O_3:C are shown in legend of Fig. 7(c). The integrated TL intensity of the optimized $NaYGeO_4$:0.003Bi^{3+},0.008 Tb^{3+} after 254 nm UV-light charging is strongest and is about 31 times higher than that of BaFBr(I):Eu^{2+}. It means that strong Tb^{3+} afterglow appears in the optimized $NaYGeO_4$:0.003Bi^{3+},0.008 Tb^{3+} after 254 nm UV-light charging, which is evidenced by the afterglow photographs in Fig. 7(d). A common TL glow peak near 327 K was observed in Bi^{3+}-codoped $NaYGeO_4$.

There is a common low temperature TL glow peak near 349 K in Fig. 7(b) and near 327 K in Fig. 7(c) whenever Bi^{3+} is present. To analyse this TL peak further we studied the $NaYGeO_4$:0.004Bi^{3+},0.005Nd^{3+} sample in more detail because it contains very low Bi^{3+} and Nd^{3+} concentration. The trapping depth (E) for $NaYGeO_4$:0.004Bi^{3+},0.005Nd^{3+} was derived by using a typical variable heating rate plot and formula [17,42,43]:

$$ln\left(\frac{T_m^2}{\beta}\right) = \frac{E}{kT_m} + ln\left(\frac{E}{ks}\right) \quad (1)$$

where k is the Boltzmann constant (8.62 × 10^{-5} eV/K), T_m is the TL glow peak, s is the frequency factor (s^{-1}), and β means the used heating rate that can adjust from 0.2 to 6.4 K/s as shown in Fig. S10. Fig. 7(e) gives the variable heating rate plot for $NaYGeO_4$:0.004Bi^{3+},0.005Nd^{3+} that determines the trap depth to be 0.78 eV and the frequency factor to be 1.23 × $10^{10}$$s^{-1}$ which is also listed in Table 1. Since the concentration of doped Bi^{3+} and Nd^{3+} is very low, it was assumed that the above obtained frequency factor s also applies to other bismuth and/or lanthanides doped $NaYGeO_4$.

Assuming a first-order TL-recombination kinetic process, the trap depth of the Bi^{2+} TL glow peak near 272 K in $NaYGeO_4$:0.004Bi^{3+} in Fig. 4(b), in $NaYGeO_4$:0.004Bi^{3+},0.005Tb^{3+} in Fig. 4(c), and in $NaYGeO_4$:0.004Bi^{3+},0.005Pr^{3+} in 4(d) can be estimated by solving Eq.

(1) with the known temperature T_m at the maximum of the TL glow curve, i.e., $T_m = 272$ K, and utilizing $s = 1.23 \times 10^{10} s^{-1}$ and $\beta = 0.2$ K/s. The trap depth for Bi^{2+} TL glow peak near 272 K is then calculated to be 0.64 eV.

Fig. 8 shows the isothermal decay curves of lanthanides and/or bismuth doped $NaYGeO_4$ after exposure to 254 nm UV-light or X-rays at RT. Fig. 8(a) shows that bright Tb^{3+} initial afterglow appears in the optimized $NaYGeO_4$:0.003Bi^{3+},0.008Tb^{3+}, which is even higher than that of the state-of-the-art $SrAl_2O_4$:Eu^{2+},Dy^{3+} and the optimized YAGG:Tb^{3+},Cr^{3+} and YAGG:Ce^{3+},Cr^{3+} transparent ceramics. Fig. 8(b) further shows that more than 27.8 h afterglow is measurable in $NaYGeO_4$:0.003Bi^{3+},0.008 Tb^{3+} after 254 nm UV-light charging. Fig. 8 (c) and 8(d) show that bright Bi^{3+} initial afterglow emerges in $NaYGeO_4$:0.004Bi^{3+}. More than 40 h afterglow is measurable in $NaYGeO_4$:0.004Bi^{3+} and the optimized $NaYGeO_4$:0.003Bi^{3+},0.008 Tb^{3+} after X-ray charging, indicating good charge carrier storage capacity after exposure to X-rays.

To unravel the charge carrier trapping processes, Fig. 9(a) and Fig. S14 show the RT isothermal decay curves of $NaYGeO_4$:0.005Tb^{3+}, $NaYGeO_4$:0.004Bi^{3+},0.005Tb^{3+}, and $NaYGeO_4$: 0.004Bi^{3+},0.005Nd^{3+} after 60 s exposure to different energy photons. Fig. 9(b)-9(d) compares the TL excitation (TLE) curves with the PL excitation (PLE) spectra of $NaYGeO_4$:0.004Bi^{3+},0.005Nd^{3+}, $NaYGeO_4$:0.005Tb^{3+}, and $NaYGeO_4$:0.004Bi^{3+},0.005Tb^{3+}. For $NaYGeO_4$:0.004Bi^{3+},0.005Nd^{3+}, it can only be charged via the Bi^{3+} D-band. For $NaYGeO_4$:0.005Tb^{3+} and $NaYGeO_4$:0.004Bi^{3+},0.005Tb^{3+}, they can be charged via Tb^{3+} 4f → 5d transition and Tb^{3+}→CB IVCT.

3.4. *Exploring anti-counterfeiting applications by using electron liberation from Bi^{2+}*

For the development of advanced applications like anti-counterfeiting and X-ray imaging, the optically stimulated luminescence and stability after exposure to water for the developed storage phosphors have been evaluated. Fig. 10(a) first shows the TL glow curves of the optimized $NaYGeO_4$:0.003Bi^{3+},0.008Tb^{3+} after exposure to X-rays with 60–1200 s duration time. The inset in Fig. 10(a) shows that the integrated TL intensity appears to linearly increase with increasing the X-ray exposure time, indicating the potential application as a dosimeter for X-ray detection. The same applies for $NaYGeO_4$:0.004Bi^{3+} in Fig. S11. Fig. 10(b) shows the TL glow curve of $NaYGeO_4$:0.003Bi^{3+},0.008Tb^{3+} after exposure to water for 1 h. The integrated TL intensity does not decrease, suggesting good chemical stability after exposure to moisture.

Optically stimulated luminescence properties are important for storage phosphors. Fig. 10(c) and S15-S16 shows the TL glow curves of $NaYGeO_4$:0.003Bi^{3+},0.008Tb^{3+} after 254 nm UV-light charging followed by different energy photon stimulation. The TL intensity decreases with 365, 396, 656, 850 nm, and WLED stimulation. It means that stored charge carriers can be removed by light stimulation. Fig. 10 (d) further shows that the stored charge carriers are removed by an optically stimulated Tb^{3+} 4f → 4f emission process. The phosphor area stimulated by illumination light like 656 nm laser in Fig. 10(e3) has less stored charge carriers and then provides less Tb^{3+} afterglow. This feature can be used to display the text of "0, 1, and a" from the $NaYGeO_4$:0.003Bi^{3+},0.008Tb^{3+} based afterglow film in the dark in Fig. 10(g1)-(g3). The similar applies for $NaYGeO_4$:0.004Bi^{3+} in Fig. S17-S18. For $NaYGeO_4$: 0.003Bi^{3+},0.008Tb^{3+}, 58% of stored charge carriers

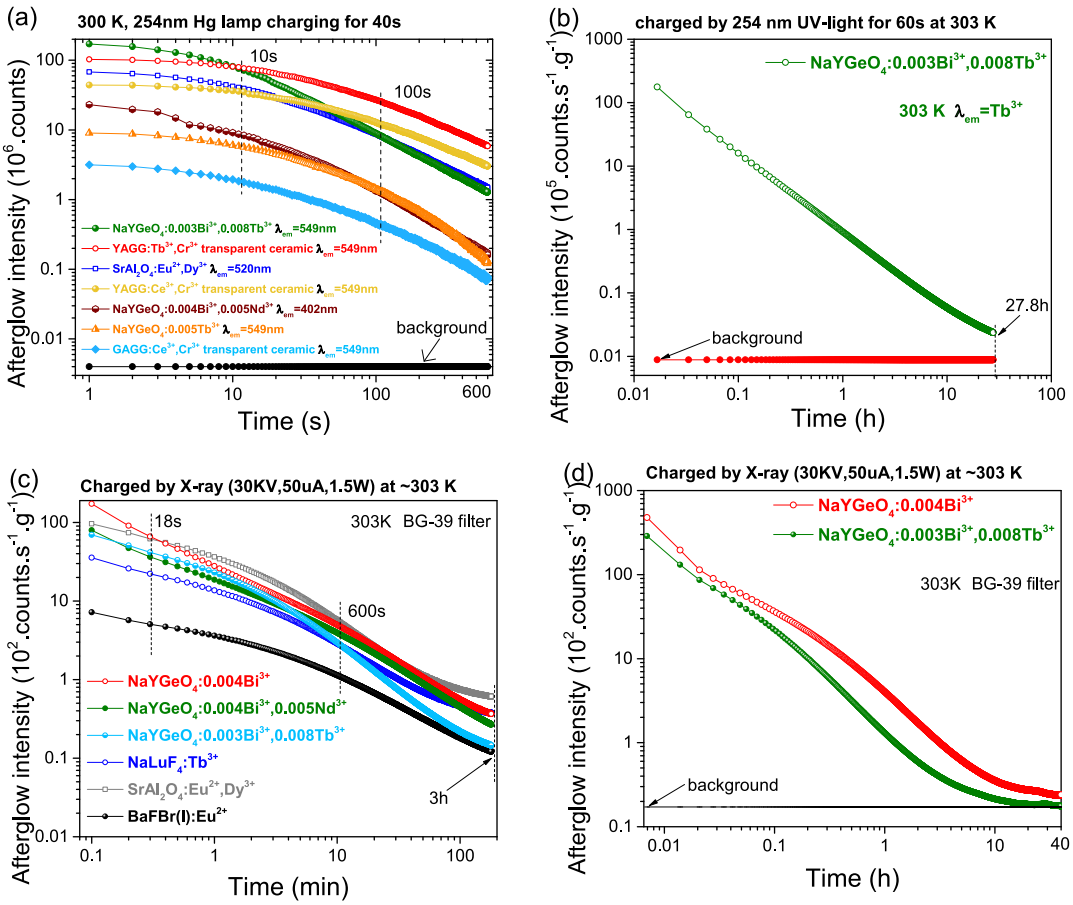

Fig. 8. (a)-(d) Isothermal decay curves of lanthanide and/or Bi^{3+} doped $NaYGeO_4$, $NaLuF_4$:Tb^{3+}, the state-of-the-art BaFBr(I):Eu^{2+}, $SrAl_2O_4$:Eu^{2+},Dy^{3+}, Al_2O_3:C single crystal chip, and transparent garnet afterglow phosphors after exposure to X-ray charging or 254 nm UV-light charging at RT (303 K).

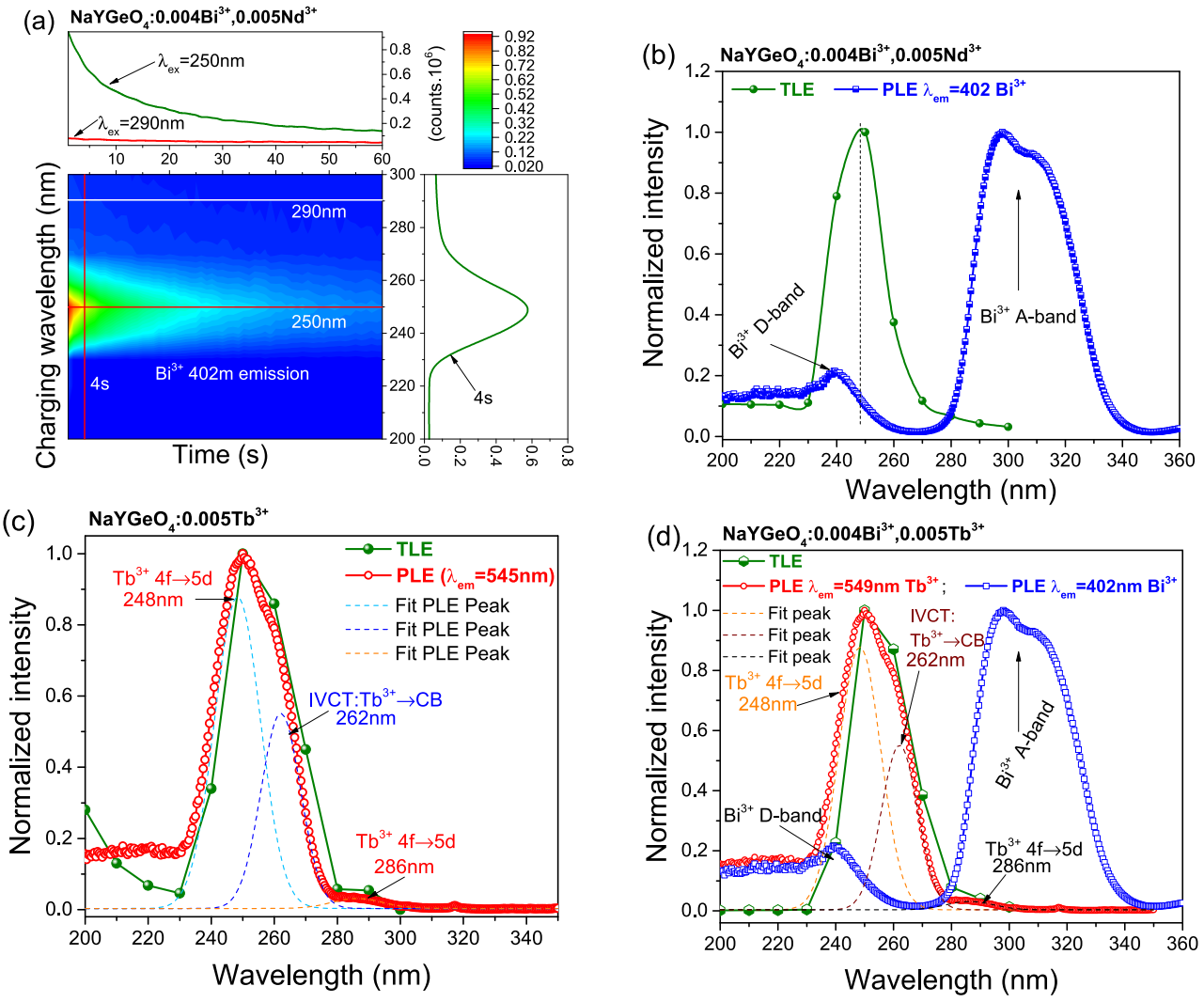

Fig. 9. (a) 2D contour plot of RT *iso*-thermal decay curves as a function of charging wavelength for $NaYGeO_4$:0.004Bi^{3+},0.005Nd^{3+}. A comparison of TL excitation (TLE) curves with the PL excitation (PLE) spectra for (b) $NaYGeO_4$:0.004Bi^{3+},0.005Nd^{3+}, (c) $NaYGeO_4$:0.005Tb^{3+}, and (d) $NaYGeO_4$:0.004Bi^{3+},0.005Tb^{3+}. The PLE spectra of $NaYGeO_4$:0.005Tb^{3+} (λ_{em} = 545 nm) and $NaYGeO_4$:0.004Bi^{3+} (λ_{em} = 402 nm) recorded at RT are also given in (c)-(d).

can be removed by 20 s WLED stimulation in Fig. 10(c). Particularly, 93% of stored charge carriers in $NaYGeO_4$:0.004Bi^{3+} can be removed by 300 s WLED stimulation as shown in Fig. S17(b), implying good optically stimulated luminescence performance.

To explore anti-counterfeiting application by using the afterglow phenomenon, Fig. S19(a)-(h) shows the afterglow photographs and persistent luminescence spectra of the optimized $NaYGeO_4$:0.003Bi^{3+},0.008Tb^{3+} and the optimized transparent garnet afterglow ceramics after exposure to 254 nm UV-light charging for 120 s. Strong afterglow photographs can be recorded for in the optimized $NaYGeO_4$:0.003Bi^{3+},0.008Tb^{3+} powder sample after removing the 254 nm UV-light for 100 s. The 100 s afterglow intensity from $NaYGeO_4$:0.003Bi^{3+},0.008Tb^{3+} is higher than that of the transparent garnet GAGG:Ce^{3+},Cr^{3+} and is comparable to that of YAGG:Tb^{3+},Cr^{3+} and YAGG:Pr^{3+},Cr^{3+} transparent garnet ceramics as shown in Fig. S19 (g).

The optimized $NaYGeO_4$:0.003Bi^{3+},0.008Tb^{3+} powder afterglow phosphor was dispersed into silicone gel to produce an afterglow film A in Fig. 11(a1)-(a5) and Fig. S20. A text of "HQU EXIT" is visible to the naked eye in the dark by selective charging the film A with a paper mask of "HQU EXIT" as demonstrated in Fig. 11(b1)-(b3). A QR code was printed on a sheet of paper as shown in Fig. 11(c1). Film A was first charged by 254 nm UV-light and then was placed underneath the sheet of the paper. Because of the strong afterglow from the optimized $NaYGeO_4$:0.003Bi^{3+},0.008Tb^{3+}, the QR code is visible in the dark and can be easily scanned by a smart mobile phone to read out the hidden information of "This is a nice persistent luminescence material" as demonstrated in Fig. 11(c1)-(c3). Fig. S19(b1)-(b3) further demonstrates that film A has good ductility by stretching it with hands. Fig. S19 (c1)-(c3) shows that the information of text of "HQU EXIT" can be stored in film A for more than 3 h and then can be read out by heating the film A to about ~ 353 K. Fig. S23(b1)-(b3) shows that afterglow film A can be stretched by hands, indicating the flexibility feature of this film.

To add new anti-counterfeiting features to film A, different concentration of $CsPbI_3$ quantum dots (QDs) was added to form film B in Fig. 12 (b1) and film C in Fig. 12(c1). The $CsPbI_3$ QDs concentration in film C is much higher than that in film B and as a result, the photoluminescence color can be tailored from dark pink to bright orange red as shown in Fig. 12(b2) and 12(c2). Efficient energy transfer from the afterglow produced by $NaYGeO_4$:0.003Bi^{3+},0.008Tb^{3+} to $CsPbI_3$ quantum dots is not observed. It means that efficient afterglow color change does not appear in film B and film C. An anti-counterfeiting application is supposed by using the highly efficient photoluminescence of $CsPbI_3$ QDs and the intense afterglow from $NaYGeO_4$:0.003Bi^{3+},0.008Tb^{3+}. This idea was testified and shown in Fig. 12(c3) and Fig. 12(c4) where the color of the text of "$CsPbI_3$ QD" can be changed from red under 254 nm

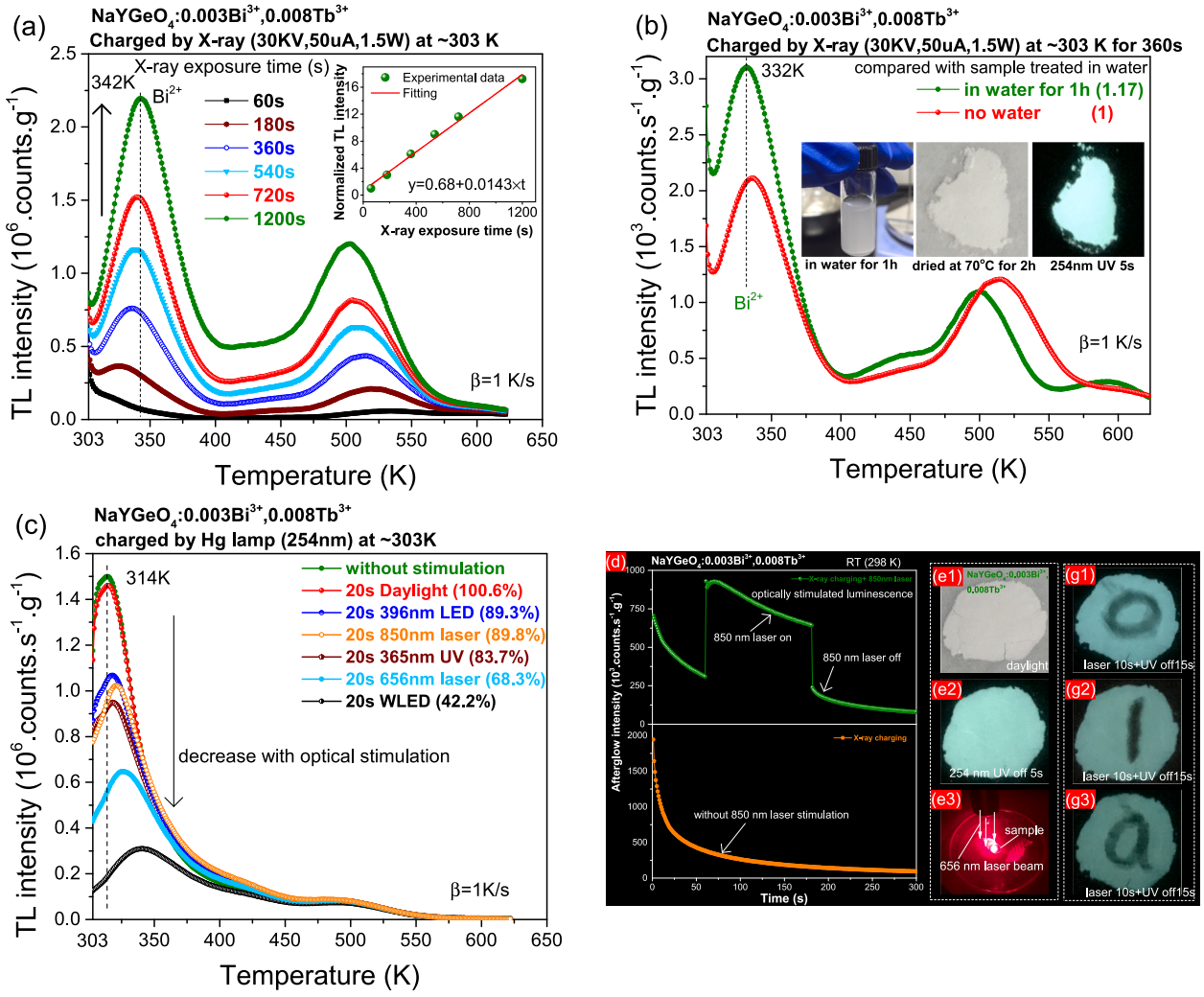

Fig. 10. TL glow curves measured at β = 1 K/s for $NaYGeO_4$:0.003Bi^{3+},0.008Tb^{3+} after exposure to (a) X-ray with different duration time, (b) water for 1 h, and (c) 20 s optical stimulation by different excitation sources. (d) RT isothermal decay curves of $NaYGeO_4$:0.003Bi^{3+},0.008Tb^{3+} after 850 nm laser stimulation. (e)-(g) Information display using the optically stimulated emission phenomenon in $NaYGeO_4$:0.003Bi^{3+},0.008Tb^{3+}.

UV-light illumination to green by stopping 254 nm UV-light illumination in the dark.

To further explore color tuning for anti-counterfeiting application, afterglow spectra were studied in bismuth and lanthanides co-doped $NaYGeO_4$. Fig. 1 predicts that, like Tb^{3+}, Pr^{3+} also can act as a hole trapping and recombination centre but then with red emission. Fig. S25 (c)-S25(d) show the RT isothermal afterglow spectra and decay curves for $NaYGeO_4$:0.004Bi^{3+},0.005Pr^{3+} after 254 nm UV-light charging. Characteristic Pr^{3+} 4f → 4f afterglow emissions appear. We therefore added Pr^{3+} in $NaYGeO_4$:Bi^{3+},Tb^{3+} to explore tailorable afterglow color. Fig. 13(a) shows the afterglow spectra of Bi^{3+} and/or lanthanides doped $NaYGeO_4$ after 254 nm UV-light charging. For $NaYGeO_4$:0.003Bi^{3+},0.008Tb^{3+},0.002Pr^{3+}, Bi^{3+} $^3P_1 \rightarrow {}^1S_0$, both Tb^{3+} and Pr^{3+} typical 4f → 4f transitions appear in 300–675 nm range as evidenced in the afterglow spectrum in Fig. 13(a) and the photoluminescence emission, excitation spectra, RT isothermal afterglow and decay curves in Fig. S25.

White afterglow with color coordinate of (0.33, 0.35) appears in $NaYGeO_4$:0.003Bi^{3+}, 0.008 Tb^{3+},0.002Pr^{3+} after 254 nm UV-light charging as shown in Fig. 13(c) and Fig. S26. Fig. S27 shows the TL glow curves of $NaYGeO_4$:0.003Bi^{3+},0.008Tb^{3+},0.002Pr^{3+} after exposure to X-ray and 254 nm UV-light. TL glow peaks near 335 K in Fig. S27 (a) and near 314 K in Fig. S27(b) emerge, which result in the white afterglow. Film D in Fig. 13(d1) was made by using $NaYGeO_4$:0.003Bi^{3+},0.008 Tb^{3+},0.002Pr^{3+} and silicone gel. A white afterglow film appears in the dark in Fig. 13(d3), which has a color coordinate of (0.30, 0.32) in Fig. 13(c). A text of "WHITE BiTbPr" appears in the dark in Fig. 13(d5) by selecting charging the film D with a paper mask in Fig. 13(d4). Fig. 13(d6) shows that about 40 h afterglow can be measurable in $NaYGeO_4$:0.003Bi^{3+},0.008 Tb^{3+},0.002Pr^{3+} after 254 nm UV-light charging.

3.5. *Exploring X-ray imaging applications by using electron liberation from Bi^{2+}*

We explored the resolution of film A in Fig. S30(a1) for X-ray imaging. A paper mask with resolution from 0.25 mm to 10 mm was made by using a sheet of paper as shown in Fig. S30(a2). Film A was placed underneath the paper mask and can be selectively charged by 254 nm UV-light in Fig. S30(a3). The afterglow photographs in Fig. S30(a4)-(a6) show that a resolution of 0.25 mm (~4 lp/mm) can be obtained from film A upon 254 nm UV-light charging. Film E was made by using $NaYGeO_4$:0.004Bi^{3+} and silicone gel. Both films A and E have been testified for X-ray imaging as shown in Fig. 14. X-ray imaging photographs for objects of capsules with a metal spring in Fig. 14(a1)-(b4), an insect in Fig. S29(a1)-(a3), a chip in Fig. S29(a4)-(a6) are visible in the dark because of the thermally stimulated luminescence of Bi^{3+} $^3P_1 \rightarrow {}^1S_0$ transition in $NaYGeO_4$:0.004Bi^{3+} from film E and Tb^{3+} 4f → 4f

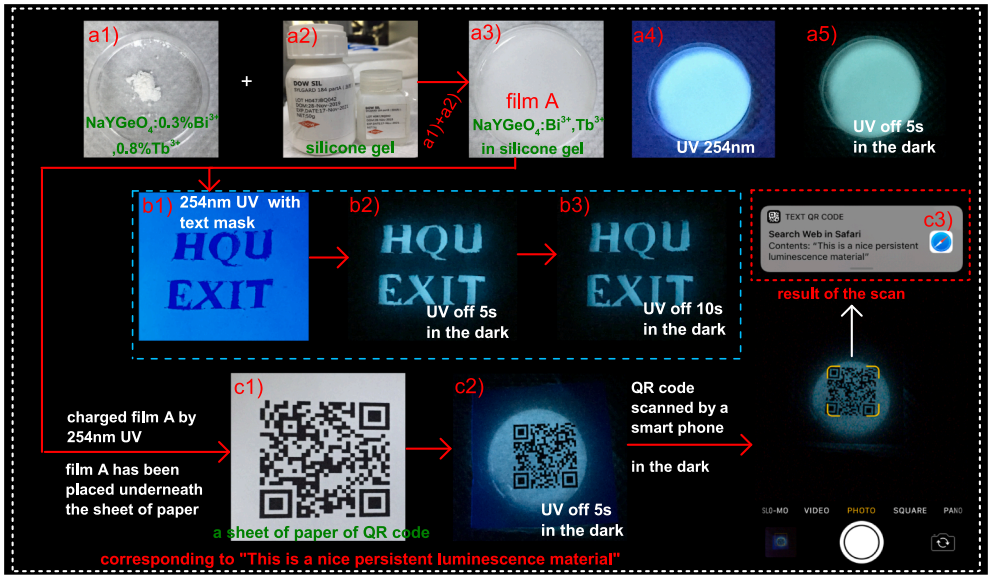

Fig. 11. Proof-of-concept anti-counterfeiting application by using $NaYGeO_4$:0.003Bi^{3+},0.008Tb^{3+} dispersed in silicone gel film A. Panels a1)-a5) show the preparation process of afterglow film A. Panels b1)-b3) and c1)–c3) show the application of the Tb^{3+} afterglow from film A to show the text of "HQU EXIT" and a QR code on a sheet of paper in the dark.

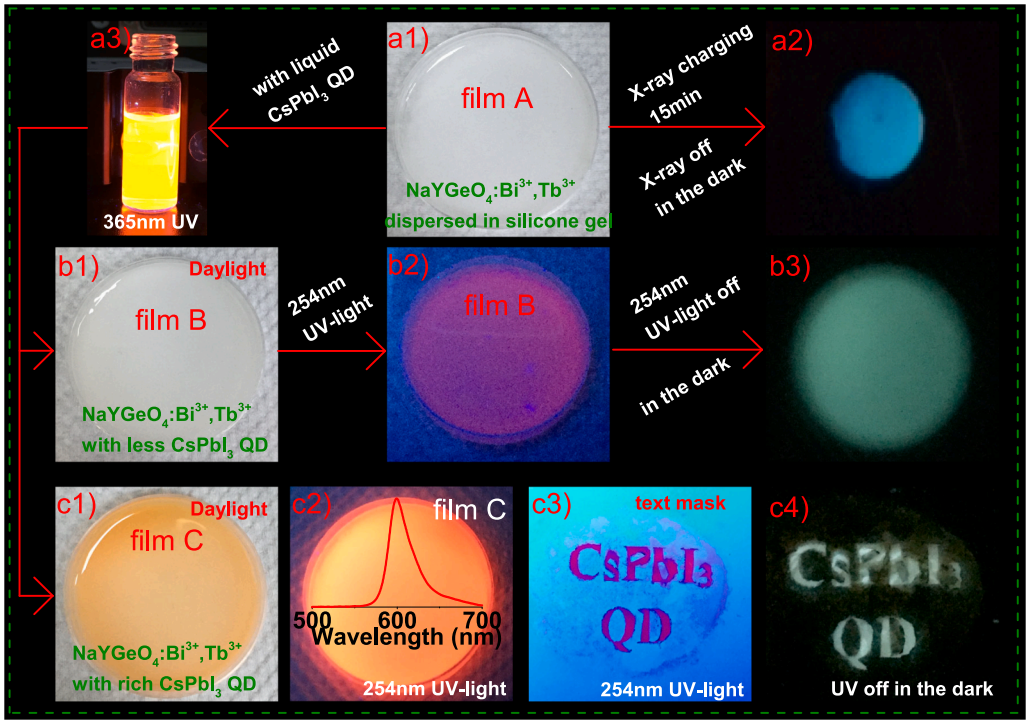

Fig. 12. Proof-of-concept anti-counterfeiting application by combining X-ray or UV-light charged Tb^{3+} afterglow and high PL quantum efficiency of $CsPbI_3$ quantum dots (QDs). a1) is $NaYGeO_4$:0.003Bi^{3+}, 0.008Tb^{3+} based film A. a2) shows the Tb^{3+} afterglow from film A after X-ray charging. a3) is the $CsPbI_3$ QD under 365 nm UV-light illumination. Panels b1)-b3) show the $CsPbI_3$-QDs-less film B and panels c1)-c4) show the $CsPbI_3$-QD-rich film C and its application to show the text of "$CsPbI_3$ QDs".

transitions in $NaYGeO_4$:0.003Bi^{3+},0.008 Tb^{3+} from film A upon heating to about 343 K. The other X-ray imaging of a chicken bone is visible in the dark as demonstrated in Fig. S28.

We further explored X-ray imaging with film A by using large electric wires and connector plugs in size of ~ 5 × 5 cm^2 as imaging object in Fig. 14(c1)-14(c4). With the increase of X-ray power from 30 W to 60 W, a X-ray imaging photograph for the electric wires and connector plugs gradually appears to be visible in the dark as shown in Fig. 14(c2)-(c4). The X-ray imaging resolution for film A was testified in Fig. 14(d1). A X-ray imaging resolution of about 3.5 lp/mm emerges in film A in the dark in Fig. 14(d2). Fig. 14(d3) shows a X-ray imaging resolution test using $(C_8H_{20}N)_2MnBr_4$ phosphor based screen. The ratio of signal to background noise in film A in Fig. 14(d2) is higher than that in $(C_8H_{20}N)_2MnBr_4$ phosphor based screen in Fig. 14(d3). The above results suggest that the developed $NaYGeO_4$:0.004Bi^{3+} and $NaYGeO_4$:0.003Bi^{3+},0.008 Tb^{3+} can be used for X-ray imaging.

4. Discussion

4.1. Electron de-trapping process from Bi^{2+} for determining VRBE at Bi^{2+} $^2P_{1/2}$

The VRBE diagram of $NaYGeO_4$ in Fig. 1(a) that was constructed in ref. [31] predicts that Bi^{3+} can act as a 0.85 ± 0.5 eV deep electron

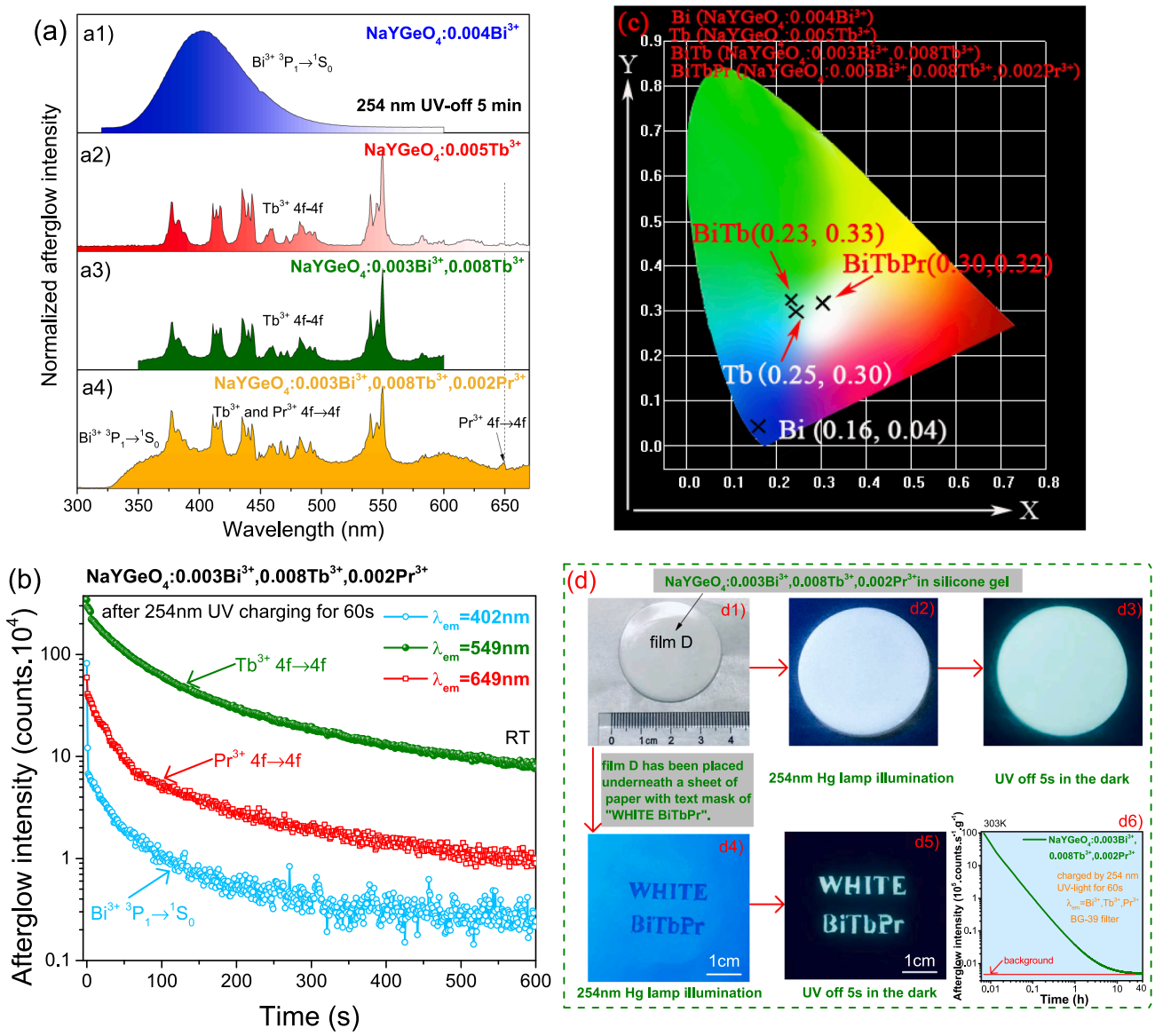

Fig. 13. (a) Afterglow spectra after 254 nm charging, (b) RT *iso*-thermal decay curves, and (c) afterglow color coordinates for lanthanide and/or Bi^{3+} doped $NaYGeO_4$. (d1)-(d5) $NaYGeO_4$:0.003Bi^{3+},0.008Tb^{3+},0.002Pr^{3+} based silicone gel afterglow film D and its application to show text of "WHITE BiTbPr" in the dark. (d6) 40 h RT *iso*-thermal decay curve for $NaYGeO_4$:0.003Bi^{3+},0.008Tb^{3+},0.002Pr^{3+}.

capturing centre, while Bi^{3+}, Ce^{3+}, Pr^{3+}, and Tb^{3+} act as 1.48 eV, 3.80 eV, 2.0 eV, and 2.13 eV deep hole capturing centres. Fig. 1 still contains a large error of ± 0.5 eV for the prediction of Bi^{2+} electron trapping depth in $NaYGeO_4$ and $NaLuGeO_4$. The predicted VRBE in the Bi^{2+} ground state in $NaYGeO_4$ and $NaLuGeO_4$ in Fig. 1 is based on the statistical result that the average VRBE in the Bi^{2+} ground state in 15 inorganic compounds emerges in the range from about −3.5 to −4 eV [45]. There are three main methods to determine the vacuum referred binding energies in the ground and excited states of Bi^{2+}. Based on the VB → Bi^{3+} charge transfer and the VRBE in the valence band (VB) of a compound, one may estimate the VRBEs in Bi^{2+} ground and excited states by further adding the energies of the characteristic Bi^{2+} transitions from $^2P_{1/2}$ to $^2P_{3/2}(1)$, $^2P_{3/2}(2)$, and $^2S_{1/2}$[46]. Katayama *et al.* used this method in ref.[47] to determine the VRBE in the Bi^{2+} ground state location in $MgGeO_3$ where a value of −3.8 eV was obtained. The second method to estimate the VRBE in the Bi^{2+} $^2P_{1/2}$ ground state is to determine the energy barrier for thermal quenching of Bi^{2+} $^2P_{3/2}$→$^2P_{1/2}$ emission in a compound[45,46,48]. Awater *et al.* used this method to determine the VRBE in Bi^{2+} $^2P_{1/2}$ ground state in $Li_2BaP_2O_7$ to −3.84 eV in ref.[46]. Unfortunately, photoluminescence of Bi^{2+} was not observed in the germanate compounds of this work and the Bi^{2+} level locations can not be derived by this method.

Fig. 1(a) predicts that the electron trap depth (0.85 ± 0.5 eV) of Bi^{3+} is about 1.33 ± 0.5 eV and ~ 0.63 ± 0.5 eV less than the hole trap depths of Bi^{3+}, Tb^{3+}, and Pr^{3+}. If this is correct, then electron liberation from Bi^{2+} and recombination with holes at Pr^{4+}, Tb^{4+}, and Bi^{4+} would give rise to a same TL glow peak but with characteristic emission from Pr^{3+}, Tb^{3+}, and Bi^{3+}. One then can estimate the Bi^{2+} $^2P_{1/2}$ ground state location by a thermoluminescence study, which is the third method to determine Bi^{2+} level location in an inorganic compound. The low-temperature TL emission (TLEM) spectra in Fig. 4 shows that a common TL glow peak near 270 K with Bi^{3+} emission in $NaYGeO_4$:0.004Bi^{3+} in Fig. 4(b), with Tb^{3+} emission in $NaYGeO_4$:0.004Bi^{3+},0.005Tb^{3+} in Fig. 4(c), and with Pr^{3+} emission in $NaYGeO_4$:0.004Bi^{3+}, 0.005Pr^{3+} in Fig. 4(d) was observed. This 270 K TL glow peak, named as Bi^{2+} TL peak, is absent in $NaYGeO_4$:0.005 Tb^{3+} in Fig. 4(a) when Bi^{3+} is absent. This indicates that there is an electron release process from Bi^{2+}. Upon thermal stimulation at about 270 K, the captured electrons are released

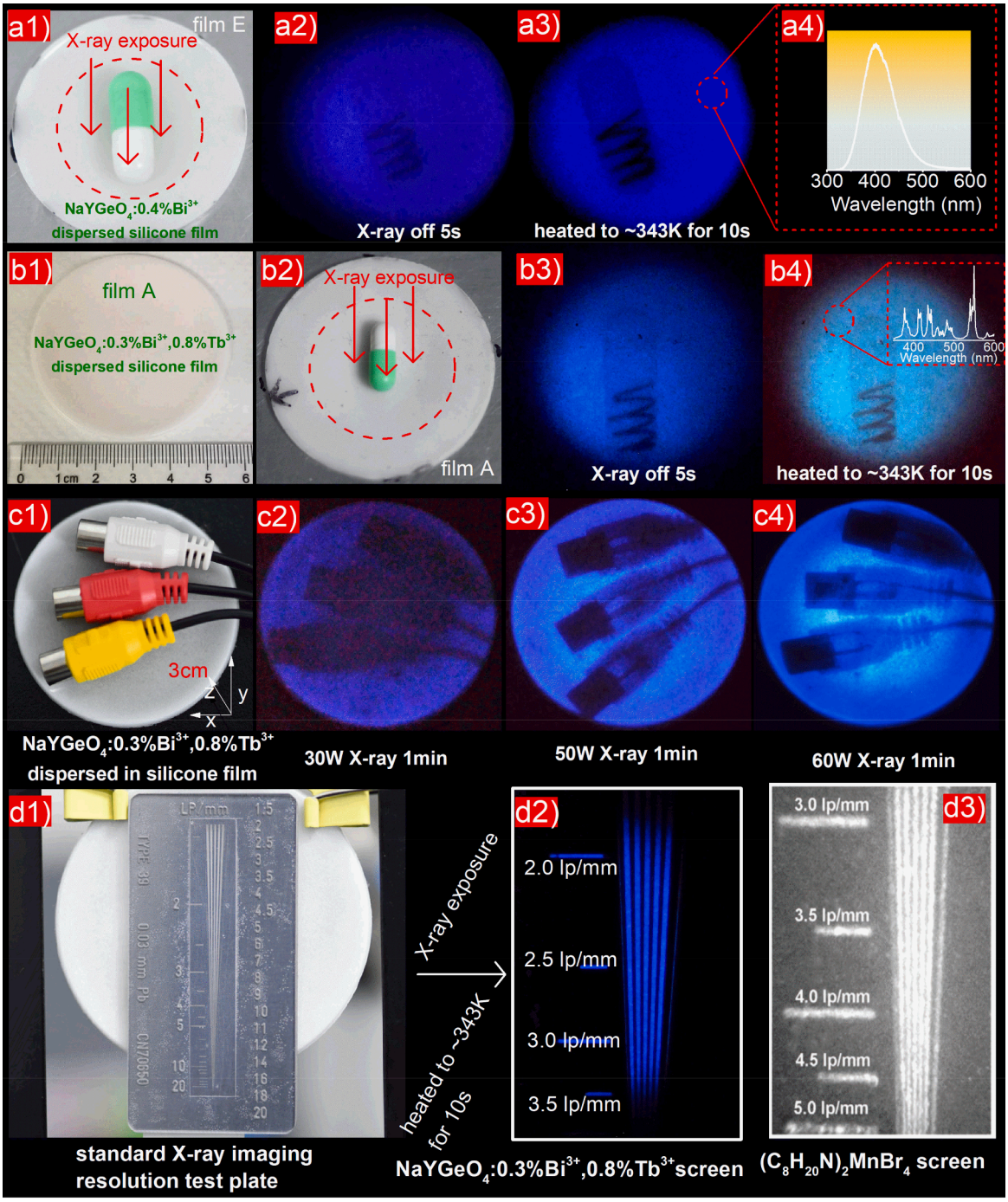

Fig. 14. Proof-of-concept X-ray imaging by using (a1)-(a4) $NaYGeO_4$:0.004Bi^{3+} based film and (b1)-(b4) $NaYGeO_4$:0.003Bi^{3+},0.008Tb^{3+} based film. (c1)-(c4) X-ray irradiation dose and (d1)-(d2) X-ray imaging resolution test for the $NaYGeO_4$:0.003Bi^{3+},0.008Tb^{3+} based optical storage film A. The thickness of the wire connectors used in (c1) is ~ 2 cm. (d3) X-ray imaging using manganese halide $(C_8H_{20}N)_2MnBr_4$ based scintillating film (reproduced with permission from Ref.[44], copyright 2021, Wiley).

from Bi^{2+} to recombine with holes trapped at Bi^{4+}, Tb^{4+}, or Pr^{4+} to produce typical Bi^{3+} $^3P_1 \rightarrow {}^1S_0$ and Tb^{3+} or Pr^{3+} 4f → 4f transitions. The electron trap depth of Bi^{3+} electron trapping centre in $NaYGeO_4$ has been calculated in Table 1 to about 0.64 eV. The VRBE in the Bi^{2+} $^2P_{1/2}$ ground state in $NaYGeO_4$ then can be deduced to ~ -3.29 eV by subtracting the trap depth from the conduction band bottom VRBE. The above obtained ~ -3.29 eV for Bi^{2+} $^2P_{1/2}$ ground state level location in $NaYGeO_4$ should be treated as indicative because the Bi^{2+} trap depth was determined based on a assumption that there is a first-order TL recombination kinetics and there is zero distribution in Bi^{2+} trapping depth. Fig. S6(c)-S6(e) demonstrated that there is a distribution in Bi^{2+} trapping depth and the Bi^{2+} trap depth increases from ~ 0.45 eV to ~ 0.80 eV with increasing T_{clean} from 308 K to 353 K in Fig. S6(e). The VRBE in the Bi^{2+} $^2P_{1/2}$ ground state in $NaYGeO_4$ can also be deduced to between ~ -3.1 and ~ -3.45 eV in $NaYGeO_4$. This value appears within the average range from ~ -3.5 eV to −4 eV for the VRBE in the Bi^{2+} ground state in inorganic compounds.

Fig. 4(b)-4(d) shows that the Bi^{3+} emission is absent in $NaYGeO_4$:0.004Bi^{3+},0.005 Tb^{3+} and $NaYGeO_4$:0.004Bi^{3+},0.005Pr^{3+}. Fig. 1 predicts that the hole trap depth of Bi^{3+} is less deep than that of

Tb^{3+} and Pr^{3+}. It means that Tb^{3+} and Pr^{3+} are more stable hole capturing centres than Bi^{3+}. During X-ray exposure, free holes prefer to be trapped by more stable Tb^{3+} and Pr^{3+} hole capturing centres, rather than by Bi^{3+} hole capturing centre. This leads to the absence of Bi^{3+} $^3P_1 \rightarrow {}^1S_0$ emission in $NaYGeO_4$:0.004Bi^{3+},0.005 Tb^{3+} and $NaYGeO_4$:0.004Bi^{3+},0.005Pr^{3+} as shown in Fig. 4(c) and 4(d). The same also applies for Fig. 13(a3) and Fig. 13(a4).

Fig. 1(b) predicts that Bi^{3+} can act as an about 0.75 ± 0.5 eV deep electron trap in $NaLuGeO_4$ and $NaYGeO_4$, and is about 1.38 ± 0.5 eV less deep than that of Tb^{3+} hole capturing centres. Fig. 1(b) further predicts that the VRBE at the conduction band bottom of $NaLuGeO_4$ is about 0.1 eV lower than that of $NaYGeO_4$. If the above predictions are correct, the Bi^{3+} electron trapping depth will increase when Lu^{3+} is substituted by Y^{3+} in $NaLu_{1-x}Y_xGeO_4$. The change of the Bi^{3+} electron trapping depth is verified by the thermoluminescence study of $NaLu_{1-x}Y_xGeO_4$:0.01Bi^{3+} in Fig. 5(a) and $NaLu_{1-x}Y_xGeO_4$:0.003Bi^{3+},0.008Tb^{3+} in Fig. 5(b) where Bi^{3+} acts as the electron trapping centre, while the Bi^{3+} in Fig. 5(a) and the Tb^{3+} in Fig. 5(b) acts as the hole trapping and recombination centres. Fig. 5(a)-5(b) shows that, with the increase of x in $NaLu_{1-x}Y_xGeO_4$:0.01Bi^{3+} and $NaLu_{1-x}Y_xGeO_4$:0.003Bi^{3+},0.008Tb^{3+}, the Bi^{2+} TL glow peak gradually shifts about 68–50 K towards higher temperature, corresponding about 0.13 eV increase of electron trap depth as listed in column 4 of Table 1. The shifting of the Bi^{2+} TL glow peak is due to the increased activation energy of electron liberation from Bi^{2+} because of conduction band rising with increasing x in $NaLu_{1-x}Y_xGeO_4$. For x = 0 in Fig. 5(b), the electron trap depth of Bi^{3+} electron trapping centre in $NaLuGeO_4$ has been determined to be ~ 0.50 eV in Table 1. The VRBE in the Bi^{2+} $^2P_{1/2}$ ground state in $NaLuGeO_4$ then can be deduced to ~ -3.22 eV by subtracting the trap depth from the conduction band bottom VRBE. This value is close to that of ~ -3.29 eV for Bi^{2+} $^2P_{1/2}$ in $NaYGeO_4$ and appears within the average range from ~ -3.5 eV to −4 eV for the VRBE in the Bi^{2+} ground state in inorganic compounds.

4.2. *Designing afterglow phosphors based on electron liberation from Bi^{2+} for anti-counterfeiting application*

For a same sample of x = 1, a TL glow peak near 283 K was observed in Fig. 5(b) and a TL glow peak near 311 K was observed in Fig. 5(c). For x = 1 in Fig. 5(c), there is 30 s delay time at 303 K between 254 nm UV-light and TL-readout. Fig. S6(c)-S6(e) have already demonstrated that there is a distribution in Bi^{2+} trapping depths in x = 1 sample. A part of stored charge carriers therefore has been faded at 303 K prior to the start of TL-readout and then a higher TL glow peak appears for x = 1 in Fig. 5 (c). The 311 K TL glow peak for x = 1 is still attributed to the electron liberation from Bi^{2+} and recombination with holes captured at Tb^{4+}. The same applies for the TL glow peaks near 303 K for x = 0–0.75 in Fig. 5(c). Fig. 5(d)-5(e) show that Tb^{3+} afterglow phosphor can be designed by using electron release from Bi^{2+} and changing x in $NaLu_{1-x}Y_xGeO_4$:0.003Bi^{3+},0.008Tb^{3+} resulting in conduction band engineering.

Fig. 7(c) shows that the integrated TL intensity of $NaYGeO_4$:0.003Bi^{3+},0.008Tb^{3+} after exposure to 254 nm UV-light is about 1.3 times higher than that of $NaYGeO_4$:0.004Bi^{3+}. After X-ray charging in Fig. 7(b), the integrated TL intensity of $NaYGeO_4$:0.004Bi^{3+} is about 4 times higher than that of $NaYGeO_4$:0.003Bi^{3+},0.008 Tb^{3+}. One should realize that charge carrier formation process induced by X-rays and UV-light charging is different. For X-ray charging, mobile free electrons and holes are created [31,49,50]. For UV-light charging, mobile electrons and holes are formed by a photo-induced ionization process from the excited states of a luminescence centre in compound like in Eu^{2+},Tm^{3+}-codoped $Ca_3Si_2O_7$ in ref.[51]. Fig. 9(b)-9(d) shows the TL excitation (TLE) plots for $NaYGeO_4$:0.005 Tb^{3+} and $NaYGeO_4$:0.004Bi^{3+},0.005 Tb^{3+}. The two phosphors can be charged via the Tb^{3+} 4f → 5d and Tb^{3+}→CB IVCT transitions or Bi^{3+} D-band. Fig. S6 (b) compares the TL glow curves for $NaYGeO_4$:0.003Bi^{3+},0.008Tb^{3+} charged by X-rays and 254 nm UV-light. The TL peak appears at ~ 30 K higher by X-ray charging than that by 254 nm UV-light charging. One possible reason is that free charge carriers created by X-rays are prefer captured by stable and deeper Bi^{2+} trapping depth since there is a distribution in Bi^{2+} trapping depth as evidenced in Fig. S6(c)-S6(e). Another possible reason is that the T_{max} is smaller when the hole and electron trap centers are close by and center-to-center recombination is expected. With photon excitation those centers are being filled preferentially. The Bi^{3+} electron trap filled with photon excitation or with X-rays can therefore be equally deep below the CB-bottom. However with center-to-center recombination the electron needs not be thermally excited to the CB. The similar applies to Bi^{3+} co-doped $NaYGeO_4$ in Fig. 7(b) and 7(c), $NaYGeO_4$:yBi^{3+},0.008 Tb^{3+} (y = 0.001–0.012) in Fig. S13(b) and S13(c), and $NaYGeO_4$:0.003Bi^{3+},0.008Tb^{3+},0.002Pr^{3+} in Fig. S27.

Because of the intense afterglow from $NaYGeO_4$:0.004Bi^{3+} and $NaYGeO_4$:0.003Bi^{3+},0.008Tb^{3+} as demonstrated in Fig. 3(h)-3(i), 8, and Fig. S19-S20, this direct afterglow can be used as illumination light source to display text and QR code in the dark as shown in Fig. 11 and S23. Color-tailorable afterglow has been explored for anti-counterfeiting application. Fig. S24 shows the PLE, PL or absorption spectra for $NaYGeO_4$:0.01Tb^{3+} and $CsPbI_3$ quantum dots (QDs). There is an overlap between the absorption spectrum of $CsPbI_3$ QDs and the PL spectrum of $NaYGeO_4$:0.01Tb^{3+} in 300–650 nm, indicating the possible energy transfer from $NaYGeO_4$:0.01Tb^{3+} to $CsPbI_3$ QDs via a reabsorption process. However, the particle size of $NaYGeO_4$:0.004Bi^{3+},0.005Tb^{3+} and $NaYGeO_4$:0.003Bi^{3+},0.008 Tb^{3+} in Fig. S1 is much larger than that of $CsPbI_3$ QDs. The re-absorption of the afterglow from $NaYGeO_4$:0.003Bi^{3+}, 0.008 Tb^{3+} by $CsPbI_3$ QDs may not efficient and this leads to the difficulty to largely tailor the afterglow color in Fig. 12.

Color-tailorable afterglow was further explored by designing electron traps, hole traps, and recombination centres in $NaYGeO_4$. Fig. 1(a) shows that the VRBE in the Nd^{2+} ground state is inside the conduction band. It means that Nd^{3+} can not act as an electron capturing centre but can act as a luminescence centre with Nd^{3+} 4f → 4f emission in the infrared range via energy transfer from Bi^{3+} to Nd^{3+} in $NaYGeO_4$[52]. This prediction is evidenced by the Bi^{3+} and Nd^{3+} infrared afterglow in Fig. 3(d) and the TLEM spectrum of $NaYGeO_4$:0.004Bi^{3+},0.005Nd^{3+} in Fig. 6(c). Fig. 1(a) predicts that Pr^{3+} can act as a hole capturing and recombination centre in $NaYGeO_4$. White afterglow appears in Bi^{3+}, Tb^{3+},Pr^{3+}-codoped $NaYGeO_4$ as demonstrated in Fig. 13 and Fig. S26-27 where Bi^{3+} acts as an electron trap, while Bi^{3+}, Tb^{3+}, and Pr^{3+} act as hole trapping and recombination centres.

4.3. *X-ray imaging application exploration*

X-ray imaging was testified by using the prepared films with different objects in Fig. 14 and S28-S29 and a resolution of 3.5 lp/mm for X-ray imaging was obtained in Fig. 14(d2). To further increase the resolution for the X-ray imaging, the particle size of the storage phosphors needs to be decreased further by ball milling or synthesizing nano-sized phosphor. The optimized $NaYGeO_4$:0.003Bi^{3+},0.008 Tb^{3+} has been further evaluated for X-ray imaging application. Fig. 10(a) shows that the integrated TL intensity for $NaYGeO_4$:0.003Bi^{3+}, 0.008Tb^{3+} increases linearly with increasing X-rays exposure time, indicating the possible application as X-rays dosimeter. Fig. 10(b) shows that $NaYGeO_4$:0.003Bi^{3+},0.008 Tb^{3+} has good chemical stability after exposure to water, which is important for practical application. Fig. 10 (c)-10(d) and S15-S18 shows that the stored charge carriers in $NaYGeO_4$:0.004Bi^{3+},0.008 Tb^{3+} and $NaYGeO_4$:0.004Bi^{3+} can be excited by different light source to generate optically stimulated Tb^{3+} and Bi^{3+} luminescence. One then may design X-ray imaging application using this feature[49].

5. Conclusions

Photoluminescence spectroscopy, vacuum referred binding energy

diagram (VRBE), and thermoluminescence technique have been combined to investigate the capturing and transport processes of electrons and holes in $NaLu_{1-x}Y_xGeO_4$ in order to develop storage phosphors for X-ray imaging and anti-counterfeiting applications. In $NaYGeO_4$:0.004Bi^{3+} and $NaYGeO_4$:0.004Bi^{3+},0.005Ln^{3+} (Ln = Tb or Pr), the Bi^{3+} ion acts as an electron capturing centre, while Bi^{3+} and Ln^{3+} act as the hole capturing and recombination centres. The trapped electrons are liberated from Bi^{2+} to recombine with holes captured at Bi^{4+} or Ln^{4+} to generate characteristic Bi^{3+} $^3P_1 \rightarrow {}^1S_0$ emission and Tb^{3+} or Pr^{3+} 4f → 4f transitions. The trap depth of Bi^{3+} electron capturing centre has been determined to about 0.64 eV by thermoluminescence study. The VRBE in the Bi^{2+} $^2P_{1/2}$ ground state is then derived to −3.29 eV in $NaYGeO_4$. The electron trap depth produced by Bi^{3+} codopant in $NaLu_{1-x}Y_xGeO_4$:0.003Bi^{3+},0.008Tb^{3+} solid solutions can be adjusted, by increasing x, resulting in conduction band engineering. Good afterglow phosphors were developed by using electron liberation from Bi^{2+} in Bi^{3+} and/or Tb^{3+} doped $NaYGeO_4$. The integrated TL intensity of the optimized $NaYGeO_4$:0.004Bi^{3+} and $NaYGeO_4$:0.003Bi^{3+},0.008Tb^{3+} after exposure to X-rays is about 4.5 and 1.1 times higher than that of the state-of-the-art BaFBr(I):Eu^{2+} storage phosphor. Intense initial Tb^{3+} 4f → 4f afterglow appears in $NaYGeO_4$:0.003Bi^{3+},0.008Tb^{3+} and more than 40 h afterglow can be measurable in $NaYGeO_4$:0.004Bi^{3+} and $NaYGeO_4$:0.003Bi^{3+},0.008Tb^{3+} after X-ray charging. We have shown proof-of-concept color tailoring for anti-counterfeiting applications by combining perovskite $CsPbI_3$ quantum dots (QD) with finely designed charge carriers in $NaYGeO_4$ where Bi^{3+} acts as an electron trap while both Tb^{3+} and Pr^{3+} act as the hole trapping and recombination centres. Proof-of-concept X-ray storage application was demonstrated in the optimized $NaYGeO_4$:0.004Bi^{3+} and $NaYGeO_4$:0.003Bi^{3+},0.008Tb^{3+} phosphors which were dispersed in the silicon gel based flexible X-ray imaging films. This work not only provides with experimental evidence on the VRBE in Bi^{2+} $^2P_{1/2}$ ground state in $NaYGeO_4$ and $NaLuGeO_4$, but also shows that how to design and develop good afterglow phosphors for anti-counterfeiting and X-ray imaging by deeply studying and controlling the trapping and de-trapping processes of charge carriers in bismuth and/or lanthanides doped inorganic compounds. Therefore, this work can accelerate the development of afterglow phosphors in a rational way instead of by the typical trial-and-error method.

Declaration of Competing Interest

The authors declare that they have no known competing financial interests or personal relationships that could have appeared to influence the work reported in this paper.

Acknowledgements

This work is financially supported by the National Natural Science Foundation of China (No. 12104170) and partly by Scientific Research Funds of Huaqiao University (No. 21BS106). We thank the support from Instrumental Analysis Center of Huaqiao University. We acknowledge Ou et al. in ref. [1] and Jian Xu for providing samples of $NaLuF_4$:Tb(15 mol%)@$NaYF_4$ and transparent (Y, Ga)$_3Al_2Ga_3O_{12}$ garnet afterglow ceramics for comparison studies in this work.

Appendix A. Supplementary data

Supplementary data to this article can be found online at https://doi.org/10.1016/j.cej.2022.135038.

References

[1] X. Ou, X. Qin, B. Huang, J. Zan, Q. Wu, Z. Hong, L. Xie, H. Bian, Z. Yi, X. Chen, Y. Wu, X. Song, J. Li, Q. Chen, H. Yang, X. Liu, High-resolution X-ray luminescence extension imaging, Nature 590 (7846) (2021) 410–415.
[2] F. Kang, G. Sun, P. Boutinaud, H. Wu, F.-X. Ma, J. Lu, J. Gan, H. Bian, F. Gao, S. Xiao, Recent advances and prospects of persistent luminescent materials as inner secondary self-luminous light source for photocatalytic applications, Chemical Engineering Journal 403 (2021), 126099.
[3] X. Wang, Y. Chen, F. Liu, Z. Pan, Solar-blind ultraviolet-C persistent luminescence phosphors, Nature Communications 11 (2020) 2040.
[4] L. Huang, L. Lin, W. Xie, Z. Qiu, H. Ni, H. Liang, Q. Tang, L. Cao, J.-X. Meng, F. Li, Near-Infrared Persistent Luminescence in a Cr3+-Doped Perovskite for Low-Irradiance Imaging, Chemistry of Materials 32 (13) (2020) 5579–5588.
[5] S. Tian, H. Zhang, X. Yang, L. Yang, Q. Min, H. Ma, X. Yu, J. Qiu, X. Xu, A dynamic three-path authenticating model for anti-counterfeiting in a single host of CaAl2Si2O8, Chemical Engineering Journal 412 (2021), 128695.
[6] X. Lin, K. Deng, H. Wu, B. Du, B. Viana, Y. Li, Y. Hu, Photon energy conversion and management in SrAl12O19: Mn2+, Gd3+ for rewritable optical information storage, Chemical Engineering Journal 420 (2021), 129844.
[7] Y.-M. Yang, Z.-Y. Li, J.-Y. Zhang, Y. Lu, S.-Q. Guo, Q. Zhao, X. Wang, Z.-J. Yong, H. Li, J.-P. Ma, Y. Kuroiwa, C. Moriyoshi, L.-L. Hu, L.-Y. Zhang, L.-R. Zheng, H.-T. Sun, X-ray-activated long persistent phosphors featuring strong UVC afterglow emissions, Light: Science & Applications 7 (2018) 88.
[8] B.-M. Liu, R. Zou, S.-Q. Lou, Y.-F. Gao, L. Ma, K.-L. Wong, J. Wang, Low-dose X-ray-stimulated LaGaO3:Sb, Cr near-infrared persistent luminescence nanoparticles for deep-tissue and renewable in vivo bioimaging, Chemical Engineering Journal 404 (2021), 127133.
[9] H. Lin, J. Xu, Q. Huang, B. Wang, H. Chen, Z. Lin, Y. Wang, Bandgap Tailoring via Si Doping in Inverse-Garnet Mg3Y2Ge3O12:Ce3+ Persistent Phosphor Potentially Applicable in AC-LED, ACS Applied Materials & Interfaces 7 (2015) 21835–21843.
[10] J.-C. Zhang, X.-Y. Xue, Y.-F. Zhu, S. Wang, H.-W. He, X. Yan, X. Ning, D. Wang, J. Qiu, Ultra-long-delay sustainable and short-term-friction stable mechanoluminescence in Mn2+-activated NaCa2GeO4F with centrosymmetric structure, Chemical Engineering Journal 406 (2021), 126798.
[11] Y. Zhuang, D. Tu, C. Chen, L. Wang, H. Zhang, H. Xue, C. Yuan, G. Chen, C. Pan, L. Dai, R.-J. Xie, Force-induced charge carrier storage: a new route for stress recording, Light: Science & Applications 9 (2020) 182.
[12] Y. Zhuang, R.-J. Xie, Mechanoluminescence Rebrightening the Prospects of Stress Sensing: A Review, Advanced Materials n/a 33 (50) (2021) 2005925.
[13] B. Tian, Z. Wang, A.T. Smith, Y. Bai, J. Li, N. Zhang, Z. Xue, L. Sun, Stress-induced color manipulation of mechanoluminescent elastomer for visualized mechanics sensing, Nano Energy 83 (2021), 105860.
[14] Y. Zhao, D. Peng, G. Bai, Y. Huang, S. Xu, J. Hao, Multiresponsive Emissions in Luminescent Ions Doped Quaternary Piezophotonic Materials for Mechanical-to-Optical Energy Conversion and Sensing Applications, Advanced Functional Materials 31 (2021) 2010265.
[15] J. Ueda, S. Miyano, J. Xu, P. Dorenbos, S. Tanabe, Development of White Persistent Phosphors by Manipulating Lanthanide Ions in Gadolinium Gallium Garnets, Advanced Photonics Research 2 (2021) 2000102.
[16] T. Matsuzawa, Y. Aoki, N. Takeuchi, Y. Murayama, A new long phosphorescent phosphor with high brightness, SrAl2O4:Eu2+, Dy3+, Journal of the Electrochemical Society 143 (1996) 2670–2673.
[17] H. Luo, A.J.J. Bos, P. Dorenbos, Controlled Electron-Hole Trapping and Detrapping Process in GdAlO3 by Valence Band Engineering, The Journal of Physical Chemistry C 120 (11) (2016) 5916–5925.
[18] T. Lyu, P. Dorenbos, Towards information storage by designing both electron and hole detrapping processes in bismuth and lanthanide-doped LiRE(Si, Ge)O4 (RE = Y, Lu) with high charge carrier storage capacity, Chemical Engineering Journal 400 (2020), 124776.
[19] T. Lyu, P. Dorenbos, Charge carrier trapping processes in lanthanide doped LaPO4, GdPO4, YPO4, and LuPO4, Journal of Materials Chemistry C 6 (2) (2018) 369–379.
[20] Y. Zhuang, L. Wang, Y. Lv, T.-L. Zhou, R.-J. Xie, Optical Data Storage and Multicolor Emission Readout on Flexible Films Using Deep-Trap Persistent Luminescence Materials, Advanced Functional Materials 28 (2018) 1705769.
[21] Y. Zhuang, Y. Lv, L. Wang, W. Chen, T.-L. Zhou, T. Takeda, N. Hirosaki, R.-J. Xie, Trap Depth Engineering of SrSi2O2N2:Ln2+, Ln3+ (Ln2+ = Yb, Eu; Ln3+ = Dy, Ho, Er) Persistent Luminescence Materials for Information Storage Applications, ACS Applied Materials & Interfaces 10 (2018) 1854–1864.
[22] P. Dorenbos, Modeling the chemical shift of lanthanide 4f electron binding energies, Physical Review B 85 (2012), 165107.
[23] H. Luo, L. Ning, Y. Dong, A.J.J. Bos, P. Dorenbos, Electronic Structure and Site Occupancy of Lanthanide-Doped (Sr, Ca)3(Y, Lu)2Ge3O12 Garnets: A Spectroscopic and First-Principles Study, The Journal of Physical Chemistry C 120 (2016) 28743–28752.
[24] J. Ueda, S. Miyano, S. Tanabe, Formation of Deep Electron Traps by Yb3+ Codoping Leads to Super-Long Persistent Luminescence in Ce3+-Doped Yttrium Aluminum Gallium Garnet Phosphors, ACS Applied Materials & Interfaces 10 (24) (2018) 20652–20660.
[25] K. Chakrabarti, V.K. Mathur, J.F. Rhodes, R.J. Abbundi, Stimulated luminescence in rare-earth-doped MgS, Journal of Applied Physics 64 (3) (1988) 1363–1366.
[26] P. Dorenbos, Electronic structure engineering of lanthanide activated materials, Journal of Materials Chemistry 22 (42) (2012) 22344, https://doi.org/10.1039/c2jm34252a.
[27] P. Dorenbos, A Review on How Lanthanide Impurity Levels Change with Chemistry and Structure of Inorganic Compounds, ECS Journal of Solid State Science and Technology 2 (2) (2013) R3001–R3011.
[28] Z. Feng, B. Lou, M. Yin, Y.-Y. Yeung, H.-T. Sun, C.-K. Duan, First-Principles Study of Bi3+-Related Luminescence and Electron and Hole Traps in (Y/Lu/La)PO4, Inorganic Chemistry 60 (7) (2021) 4434–4446.
[29] H.-T. Sun, J. Zhou, J. Qiu, Recent advances in bismuth activated photonic materials, Progress in Materials Science 64 (2014) 1–72.

[30] T. Lyu, P. Dorenbos, Bi3+ acting both as an electron and as a hole trap in La-, Y-, and LuPO4, Journal of Materials Chemistry C 6 (23) (2018) 6240–6249.
[31] T. Lyu, P. Dorenbos, Vacuum referred binding energies of bismuth and lanthanide levels in ARE(Si, Ge)O4 (A=Li, Na; RE=Y, Lu); towards designing charge carrier trapping processes for energy storage, Chemistry of Materials 32 (2020) 1192–1209.
[32] J. Xu, S. Tanabe, Persistent luminescence instead of phosphorescence: History, mechanism, and perspective, Journal of Luminescence 205 (2019) 581–620.
[33] J. Xu, J. Ueda, S. Tanabe, Novel persistent phosphors of lanthanide-chromium co-doped yttrium aluminum gallium garnet: design concept with vacuum referred binding energy diagram, Journal of Materials Chemistry C 4 (2016) 4380–4386.
[34] J. Xu, J. Ueda, K. Kuroishi, S. Tanabe, Fabrication of Ce3+–Cr3+ co-doped yttrium aluminium gallium garnet transparent ceramic phosphors with super long persistent luminescence, Scripta Materialia 102 (2015) 47–50.
[35] J. Xu, S. Tanabe, A.D. Sontakke, J. Ueda, Near-infrared multi-wavelengths long persistent luminescence of Nd3+ ion through persistent energy transfer in Ce3+, Cr3+ co-doped Y3Al2Ga3O12 for the first and second bio-imaging windows, Applied Physics Letters 107 (2015), 081903.
[36] X. Wang, Z. Bao, Y.-C. Chang, R.-S. Liu, Perovskite Quantum Dots for Application in High Color Gamut Backlighting Display of Light-Emitting Diodes, ACS Energy Letters 5 (11) (2020) 3374–3396.
[37] M. Lu, X. Zhang, X. Bai, H. Wu, X. Shen, Y.u. Zhang, W. Zhang, W. Zheng, H. Song, W.W. Yu, A.L. Rogach, Spontaneous Silver Doping and Surface Passivation of CsPbI3 Perovskite Active Layer Enable Light-Emitting Devices with an External Quantum Efficiency of 11.2%, ACS Energy Letters 3 (7) (2018) 1571–1577.
[38] X. Wang, C. Heng, Z. Qiao, L. Ning, First-principles study on luminescent properties of Bi3+-doped ALuGeO4 (A = Li, Na): Insights into effects of host cation on emission wavelength, Journal of Luminescence 244 (2022), 118700.
[39] Z. Qiao, X. Wang, C. Heng, W. Jin, L. Ning, Exploring Intrinsic Electron-Trapping Centers for Persistent Luminescence in Bi3+-Doped LiREGeO4 (RE = Y, Sc, Lu): Mechanistic Origin from First-Principles Calculations, Inorganic Chemistry 60 (2021) 16604–16613.
[40] B. Lou, J. Wen, L. Ning, M. Yin, C.-G. Ma, C.-K. Duan, Understanding the defect levels and photoluminescence in a series of bismuth-doped perovskite oxides: First-principles study, Physical Review B 104 (11) (2021), https://doi.org/10.1103/PhysRevB.104.115101.
[41] K. Van den Eeckhout, A.J.J. Bos, D. Poelman, P.F. Smet, Revealing trap depth distributions in persistent phosphors, Physical Review B 87 (2013), 045126.
[42] W. Hoogenstraaten, Electron traps in zinc–sulphide phosphors, Philips Res. Rep 13 (1958) 515–693.
[43] J. Azorín, Determination of thermoluminescence parameters from glow curves—I. A review, International Journal of Radiation Applications and Instrumentation. Part D, Nuclear Tracks and Radiation Measurements 11 (3) (1986) 159–166.
[44] T. Jiang, W. Ma, H. Zhang, Y. Tian, G. Lin, W. Xiao, X. Yu, J. Qiu, X. Xu, Y. Yang, D. Ju, Highly Efficient and Tunable Emission of Lead-Free Manganese Halides toward White Light-Emitting Diode and X-Ray Scintillation Applications, Advanced Functional Materials 31 (2021) 2009973.
[45] R.H.P. Awater, P. Dorenbos, Towards a general concentration quenching model of Bi3+ luminescence, Journal of Luminescence 188 (2017) 487–489.
[46] R.H.P. Awater, P. Dorenbos, X-ray Induced Valence Change and Vacuum Referred Binding Energies of Bi3+ and Bi2+ in Li2BaP2O7, The Journal of Physical Chemistry C 120 (28) (2016) 15114–15118.
[47] Y. Katayama, J. Ueda, S. Tanabe, Effect of Bi2O3 doping on persistent luminescence of MgGeO3:Mn2+ phosphor, Opt. Mater. Express 4 (2014) 613–623.
[48] R.H.P. Awater, L.C. Niemeijer-Berghuijs, P. Dorenbos, Luminescence and charge carrier trapping in YPO4:Bi, Optical Materials 66 (2017) 351–355.
[49] P. Leblans, D. Vandenbroucke, P. Willems, Storage Phosphors for Medical Imaging, Materials 4 (2011) 1034.
[50] M. Thoms, H. von Seggern, A. Winnacker, Spatial correlation and photostimulability of defect centers in the x-ray-storage phosphor BaFBr:Eu2+, Physical Review B 44 (1991) 9240–9247.
[51] J. Ueda, R. Maki, S. Tanabe, Vacuum Referred Binding Energy (VRBE)-Guided Design of Orange Persistent Ca3Si2O7:Eu2+ Phosphors, Inorganic Chemistry 56 (17) (2017) 10353–10360.
[52] T. Lyu, P. Dorenbos, Designing thermally stimulated 1.06 μm Nd3+ emission for the second bio-imaging window demonstrated by energy transfer from Bi3+ in La-, Gd-, Y-, and LuPO4, Chemical Engineering Journal 372 (2019) 978–991.